近赤外光を用いた光計測の高度化に関する研究

2023 年 3 月

是澤 秀紀

Outline of PhD thesis

Study on advancement of optical measurement using near-infrared light

January, 2023
Hidenori Koresawa

Index

1. Introduction

Near-infrared (NIR) light lays within a wavelength range of 780-2500 nm, which is longer wavelength than visible light and is invisible to human eyes. About 50% of sunlight reaching the ground is occupied by NIR light, and it is used in familiar applications such as remote control of air conditioner and wireless communications. Also, NIR light is used for nondestructive testing since it is a low-photon-energy electromagnetic wave and hence causes little damage to samples. Furthermore, NIR light is also applied for medical applications. While water absorption is largely suppressed in NIR light compared with mid-infrared light due to less absorption lines, scattering of NIR light is less than that of visible or ultraviolet light, allowing deeper penetration to materials without any damages. From those characteristics, NIR light has a potential to enhance the performance of various optical measurements.

In this PhD thesis, we aim to advance three kinds of optical measurements by use of NIR light. This PhD thesis is organized by the following three topics.

(1) Lock-in-detection dual-comb spectroscopy [1]

(2) Dynamic characterization of polarization property in liquid-crystal-on-silicon spatial light modulator using dual-comb spectroscopic polarimetry [2]

(3) Hybrid angular-interrogation surface plasmon resonance sensor based on beam-angle-scanning angular spectrum and beam-angle-fixed reflectance in the near-infrared region for wide dynamic range refractive index sensing [3, 4]

In the first topic of this PhD thesis, we use an optical frequency comb (OFC) [5-7] as the NIR light for enhancement of dual-comb spectroscopy (DCS) [8-11]. DCR is useful for gas spectroscopy due to the high potential of OFC. However, fast Fourier transform (FFT) calculation of a huge amount of temporal data spends significantly longer time than the acquisition time of an interferogram. In this topic, we demonstrate frequency-domain DCS by a combination of DCS with lock-in detection, namely LID-DCS. LID-DCS directly extracts an arbitrary OFC mode from a vast number of OFC modes without the need for FFT calculation. Usefulness of LID-DCS is demonstrated in the rapid monitoring of transient signal change and spectroscopy of hydrogen cyanide gas.

In the second topic of this PhD thesis, we introduce DCS of NIR optical comb in spectroscopic polarimetry (SP). SP is a powerful tool for characterization of thin film, polarization optics, semiconductor, and others [12-22]. However, mechanical polarization modulation of broadband light hampers its application for dynamic monitoring of a sample. In this topic, we demonstrate the dynamic SP with features of polarization-modulation-free polarimetry and spectrometer-free spectroscopy benefiting from DCS using a pair of OFCs. DCS enables the direct determination of polarization without the need for polarization modulation by using mode-resolved OFC spectra of amplitude and

phase for two orthogonally linear-polarized lights while securing rapid, high-precision, broadband spectroscopy without the need for spectrometer [23]. Effectiveness of the proposed system is highlighted by visualizing the hysteresis property of dynamic response in a liquid-crystal-on-silicon spatial light modulator at a sampling rate of 105 Hz.

In the third topic of this PhD thesis, we use CW light in NIR region for highly sensitive surface plasmon resonance (SPR) sensors. SPR sensors are powerful tools for optical sensing of refractive index (RI) and bio-molecules due to their high sensitivity [24-28]. In this article, we demonstrate a beam-angle-scanning SPR system using a combined galvanometer mirror and relay lens optics. Use of a photodetector in the galvanometer mirror scanning of the incident beam angle enables both high precision and rapid data acquisition. RI resolution of 3.27×10^{-6} refractive index unit (RIU) and RI accuracy of 1.68×10^{-4} RIU were achieved at a data acquisition rate of 100 Hz. The results show the high potential of this beam-angle-scanning SPR system.

2. Lock-in-detection dual-comb spectroscopy

2.1. Introduction

Fourier transform infrared spectroscopy (FT-IR) is widely used for gas spectroscopy because of sensitive and no-requirement for sample preparation required in gas chromatography. In FT-IR, acquisition rate depends on a scanning speed of optical pathlength whereas spectral resolution is determined by an inverse of scanned optical pathlength. Use of mechanical stage for scanning of optical pathlength in FT-IR hampers slow acquisition rate and low spectral resolution. To overcome these problems, we focused on a near-infrared light source called an optical frequency comb (OFC) [5-7]. OFC enable us to benefit from a group of a vast number of phase-locked narrow-linewidth continuous-wave (CW) lights with a constant frequency spacing f_{rep} (typically, 50 to 100 MHz) over a broad spectral range. The inherent mode-locking nature and active laser control make it possible to use the OFC as an optical frequency ruler traceable to a microwave or radio-frequency (RF) frequency standard. To fully utilize both its narrow spectral linewidth and broadband spectral coverage for broadband spectroscopy, it is essential to acquire the mode-resolved OFC spectrum. Dual-comb spectroscopy (DCS) [8-11] is a technique for acquiring the mode-resolved OFC spectrum via its replica in RF regions, namely RF combs, by using dual OFCs with slightly mismatched frequency spacing (= f_{rep1} and f_{rep2}). Since DCS is more rapid, precise, and accurate acquisition of the spectrum than FTIR, DCS-based gas analysis has several advantages over conventional gas analysis including gas chromatography: real-time data acquisition, simultaneous analysis of multiple gasses, and no need for sample preparation. For example, the broad-band DCS covering from 158 to 300 THz, corresponding to 1.0 to 1.9 μm, has been effectively applied for simultaneous analysis of acetylene, methane, and water vapor [39]. Also, DCS has been used for monitoring of atmospheric gas [40,41] and gas turbine exhaust [42]. Furthermore, such DCS has been extended to the mid-infrared region [43] and even the terahertz (THz) region [44,45].

In usual DCS, after a temporal waveform of a single interferogram or consecutive interferograms was acquired in time domain, mode-resolved OFC spectrum is obtained by fast Fourier transform (FFT) calculation of the acquired temporal waveform. However, FFT calculation consumes time due to a huge amount of temporal data for the mode-resolved OFC spectra. Due to this FFT calculation, the actual measurement rate significantly decreases even though the acquisition rate of temporal waveform can be increased up to a difference of f_{rep} between dual OFCs (= $\Delta f_{rep} = f_{rep2} - f_{rep1}$); it will hamper monitoring of transient signal change. Low duty factor in the ultra-discrete tooth-like spectrum of OFC is another practical limitation of DCS. For example, when the mode-resolved OFC spectrum is measured by a spectral resolution of $f_{rep}/100$, the mode linewidth of the measured OFC spectrum is decreased down to $f_{rep}/100$. However, spectral data points except mode peaks fall in gap regions between OFC modes; only 1% of the spectral data points gives the information on the signal of mode

peaks, and the remaining 99% of them gives no information due to noise region without OFC modes. Furthermore, in the case of gas spectroscopy, the absorption lines of the gas molecule are localized at specific spectral region [39]; it is not always necessary to acquire the whole spectral range of OFC, and only the spectral information at the absorption lines is sufficient for simple analysis. Therefore, the spectral analysis with minimum required spectral information is greatly desired for efficient and fast DCS.

One possible method of overcoming these limitations is the frequency-domain acquisition in DCS by use of lock-in detection (LID). Since the RF comb has a highly stable, discrete spectrum in frequency domain, one can extract only a specific RF comb mode by selection of a LID reference frequency; simultaneously, other unnecessary RF comb modes and gap data points can be rejected. This leads to the great reduction of the data size. More importantly, since the LID is based on the frequency-domain measurement, it needs no FFT calculation to obtain the spectral information, enabling fast processing in DCS. Its acquisition time is dependent on a LID time constant independently of Δf_{rep}. Combination of LID with DCS, namely LID-DCS, has been successfully demonstrated in DCS-based distance measurement, in which the optical phase of the specific RF comb mode was measured by LID [46,47]. However, there are no attempts to apply LID-DCS for gas spectroscopy requiring the optical amplitude measurement of specific RF comb mode.

In this topic of this PhD thesis, we evaluate the basic performance of LID-DCS by comparing with usual DCS from viewpoint of net measurement time and signal-to-nose ratio (SNR). We further demonstrate use of LID-DCS for spectroscopy of hydrogen cyanide gas.

2.2. Experimental setup

Figure 2.1(a) shows a principle of operation in LID-DCS. In the frequency-domain description of DCS, two OFCs with a slightly different repetition frequency (signal OFC, mode spacing = f_{rep1} ; local OFC, mode spacing = $f_{rep2} = f_{rep1} + \Delta f_{rep}$) generates a secondary frequency comb in RF region, namely RF comb (mode spacing = Δf_{rep}), via the multi-frequency heterodyning interference between them. In usual DCS, the RF comb is acquired as an RF interferogram in time domain and then is obtained as the mode-resolved spectrum by FFT calculation of the RF interferogram. In LID-DCS, a lock-in amplifier (LIA) enables us to acquire both amplitude and phase of a frequency signal synchronized with a LID reference-frequency signal. Therefore, one can select an arbitrary mode from the mode-resolved RF comb spectrum without the need for FFT calculation by tuning the LID reference frequency to coincide with a target RF-comb-mode frequency.

Figure 2.1(b) shows an experimental setup of LID-DCS, which is based on the free-space optical setup except light sources. The reason for use of the free-space optical setup is in the flexibility of the setup construction. Two mode-locked erbium-doped fiber combs (OCLS-HSC-D100-TKSM, Neoark Co., Japan; center wavelength = 1560 nm, spectral bandwidth = 50 nm; signal OFC, carrier-envelope-

offset frequency = f_{ceo1} = 10.5 MHz, f_{rep1} = 100.000188 MHz ; local OFC, f_{ceo2} = 10.5 MHz, f_{rep2} = 99.999976 MHz; $\Delta f_{rep} = f_{rep2} - f_{rep1}$ = 212 Hz) were used for light sources in LID-DCS. We used a rubidium frequency standard (Rb-FS, Stanford Research Systems, Inc., FS725; frequency = 10 MHz, accuracy = 5×10^{-11}; instability = 2×10^{-11} at 1 s) for a frequency reference in these dual OFCs. The local OFC, equipped with an intra-cavity electro-optical modulator for laser control, was tightly and coherently locked to the signal OFC with a frequency offset using a narrow-linewidth continuous-wave (CW) laser (CWL, Redfern Integrated Optics, Inc., Santa Clara, California, USA, PLANEX; center wavelength = 1550 nm; FWHM < 2.0 kHz) for an intermediate laser [48,49]. Polarization of the signal OFC light and the local OFC light was aligned at the vertical direction by use pairs of a quarter waveplate (λ/4) and a half waveplate (λ/2). After spatially overlapping of them for optical interference by a beam splitter (BS), the dual OFC lights passed through a band-pass filter (BPF, pass band = 1550 ± 10 nm) for bandwidth reduction and another λ/2 for polarization rotation by 45°. Then, the dual OFC lights were split for a signal light and a reference light by a polarization beam splitter (PBS). A sample was placed into the optical path of the signal light. The RF combs of the signal light and the reference light, namely signal RF comb and reference one, were respectively detected by a pair of photodetectors (PDs, Thorlabs, PDA10CF-EC; wavelength = 800–1700nm; bandwidth < 150 MHz). We extract an arbitrary comb mode from the signal RF comb by a radio-frequency LIA (RF-LIA1, Stanford Research Systems, SR844; frequency range = 25kHz ~ 200 MHz, time constant = no or 100 μs to 30 ks). We further extracted the same-order comb mode of the reference RF comb for a reference to compensate the common-mode fluctuation in amplitude, arising from dual OFC and/or environmental disturbance, by use of another RF-LIA (RF-LIA2, Stanford Research Systems, SR844) in real-time. Then, we calculated amplitude ratio between them as a normalized amplitude spectrum. LID reference-frequency signals for RF-LIA1 and RF-LIA2 were generated from a RF waveform generator (RF-WG, Keysight Technologies, 33510B, frequency range < 20 MHz). Since dual OFCs and the RF-WG share the same Rb-FS for the common frequency reference, the LID reference-frequency signal can be synchronized with the arbitrary RF comb mode.

For comparison with LID-DCS, we performed usual DCS using the same optical setup except the reference light in Fig. 1(b). The detected electrical signal was acquired using a digitizer (National Instruments Corp., NI PXIe-5122; resolution = 14 bit). The sampling clock signal was synchronized with frep2. We made an FFT calculation program to obtain full spectrum of amplitude and phase in OFC with LabView2017 (National Instruments Corp., 64 bit) and performed it in a computer (National Instruments Corp., PXIe-8840, Intel Core i7, Processor base frequency = 2.60 GHz, Cache = 6 MB smart cache, RAM = 8GB).

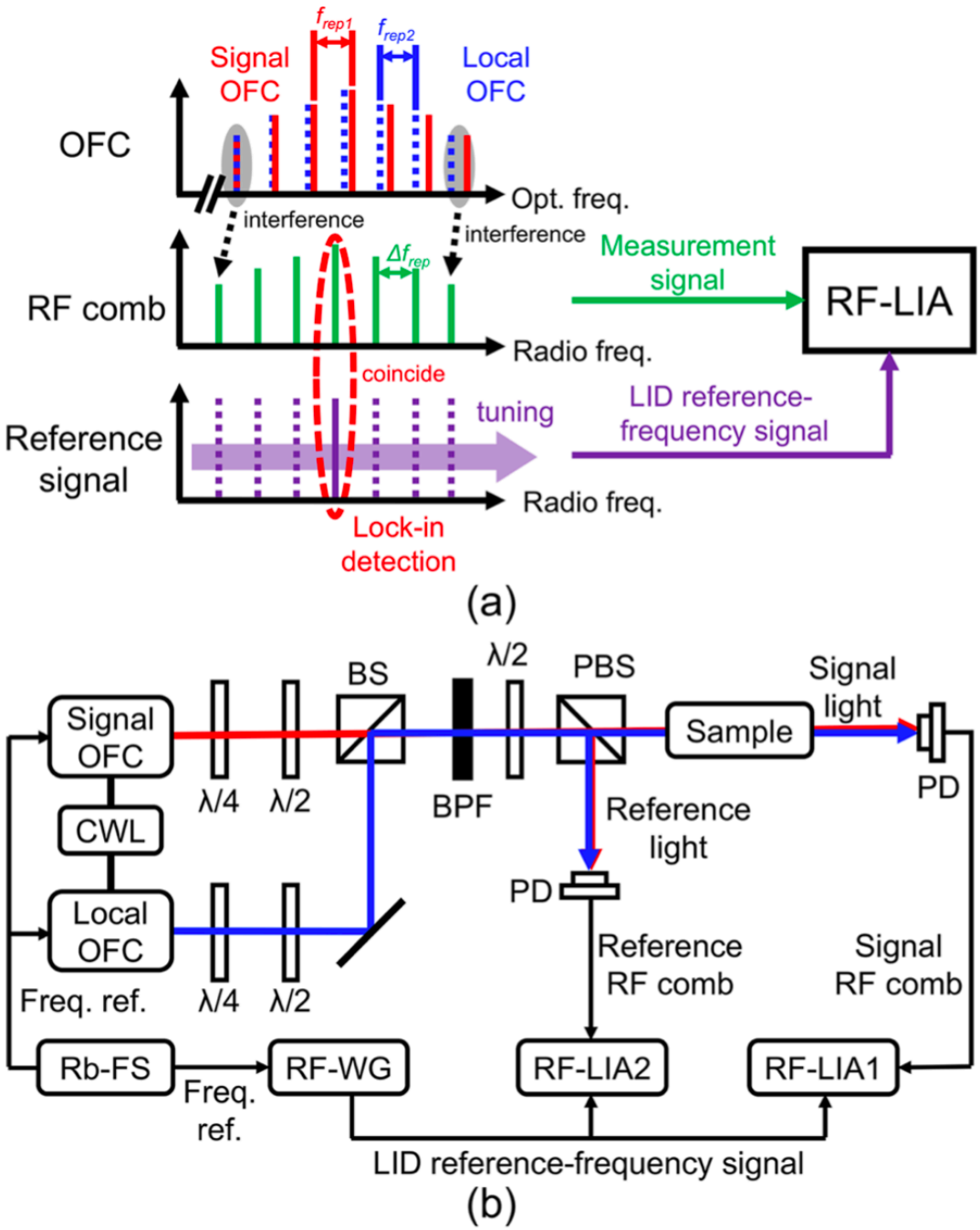

Fig. 2.1. (a) Principle of operation and (b) experimental setup of LID-DCS. Signal and local OFCs, signal and local optical frequency combs; CWL, narrow-linewidth CW laser; Rb-FS, rubidium frequency standard; λ/4, a quarter waveplate; λ/2, half waveplate; BS, beam splitter; BPF, 1550 ± 10 nm band-pass filter; PBS, polarization beam splitter; PD, photodetector; RF-LIA1 and RF-LIA2, radio-frequency lock-in amplifiers; RF-WG, RF waveform generator.

2.3. Result

2.3.1. Performance evaluation of LID-DCS

Before performing the performance evaluation, we defined the net measurement time and optical spectral resolution in the following experiments. The net measurement time of LID- DCS was defined as an acquisition time of accumulated signal, and was given in the unit of "ms/spectral_point" because LID-DCS gives a single point in the spectrum; that of DCS was defined as a sum of acquisition time of interferogram and its FFT calculation time, and was given in the unit of "ms/spectrum" because DCS gives the whole spectrum. On the other hand, the optical spectral resolution of LID-DCS was calculated by the product of LID spectral resolution { = 1/[2π*(LID time constant)]} and the frequency-scale conversion factor (= $f_{rep1}/\Delta f_{rep}$); that of DCS was given by an inverse of time window size in the interferogram. We first measured a fluctuation of spectral amplitude at a certain optical frequency in LID-DCS and DCS when the net measurement time of a single spectral point in LID-DCS (= 42 ms) was set to be equal to the acquisition time of 9 consecutive interferogram in DCS (= 42 ms) while maintaining the same optical spectral resolution in them. Figures 2.2(a) and 2.2(b) compare a fluctuation of spectral amplitude at 193.554964 THz between LID-DCS (optical spectral resolution=10.8 MHz, LID time constant=3ms, number of signal accumulation=14, net measurement time = 42 ms/spectral_point) and DCS (optical spectral resolution = 11.1 MHz, number of consecutive interferograms = 9, time window size = $9/f_{rep1}$ = 90 ns, sampling time interval = $1/f_{rep2}$ - $1/f_{rep1}$ = 21.2 fs, number of temporal data = 4,716,980, acquisition time of interferogram = $9/\Delta f_{rep}$ = 42 ms/data, number of interferogram accumulation = 1, FFT calculation time = 3.08 s/data, net measurement time = 3.12 s/spectrum) with respect to the number of measured data. Similar fluctuation of spectral amplitude was observed in both. When we defined SNR as a ratio of the mean to the standard deviation in spectral amplitude, SNR in them is significantly similar to each other: 30.6 for LID-DCS and 31.9 for DCS. Therefore, use of LID in DCS does not contribute to negative effect in SNR. Although the total number of data plots was equal to each other in Figs. 2.2(a) and 2.2(b), there is a large difference of the net measurement time between them if the total number of measured data is converted into the total net measurement time: 2.8 s for LID-DCS and 206 s for DCS. The net measurement time of LID-DCS is determined by the LID time constant and the number of signal accumulation; in DCS, most of the net measurement time is occupied by the FFT calculation time rather than the acquisition time of interferogram.

Considering the results in Figs. 2.2(a) and 2.2(b), the LID-DCS can reduce the net measurement time while maintaining the SNR and the spectral resolution similar to DCS. Figure 2.2(c) compares SNR of spectral amplitude at 193.559964 THz with respect to the net measurement time between LID-DCS (see red circle) and DCS (see blue circle). We here adjusted the optical spectral resolution of DCS while maintaining the constant optical resolution of LID-DCS to match the net measurement time of LID-DCS and that of DCS (see red and blue triangles). The linear relation was confirmed between SNR and net measurement time in both methods. Starting point of the slope in LID-DCS (see

red line) was significantly higher SNR and shorter net measurement time than that in DCS because of no FFT calculation. The slope coefficient was determined to be 0.37 for LID-DCS and 0.57 for DCS, respectively. In LID-DCS, while the residual timing jitter between dual OFCs somewhat fluctuates frequency of RF comb modes, the LID reference frequency is always fixed at a constant value. Lock-in detection of such frequency-fluctuated signal at a fixed frequency makes the LID-DCS sensitive to the timing jitter and hence limits the slope coefficient. In the case of DCS, we applied the phase compensation for the RF interferogram, in which the phase of the RF interferogram was preset to null for every interferogram by the self-triggering of the RF interferogram in the acquisition of temporal waveform, making DCS robust to the residual timing jitter. Difference of slope coefficient between LID-DCS and DCS is mainly due to these effects.

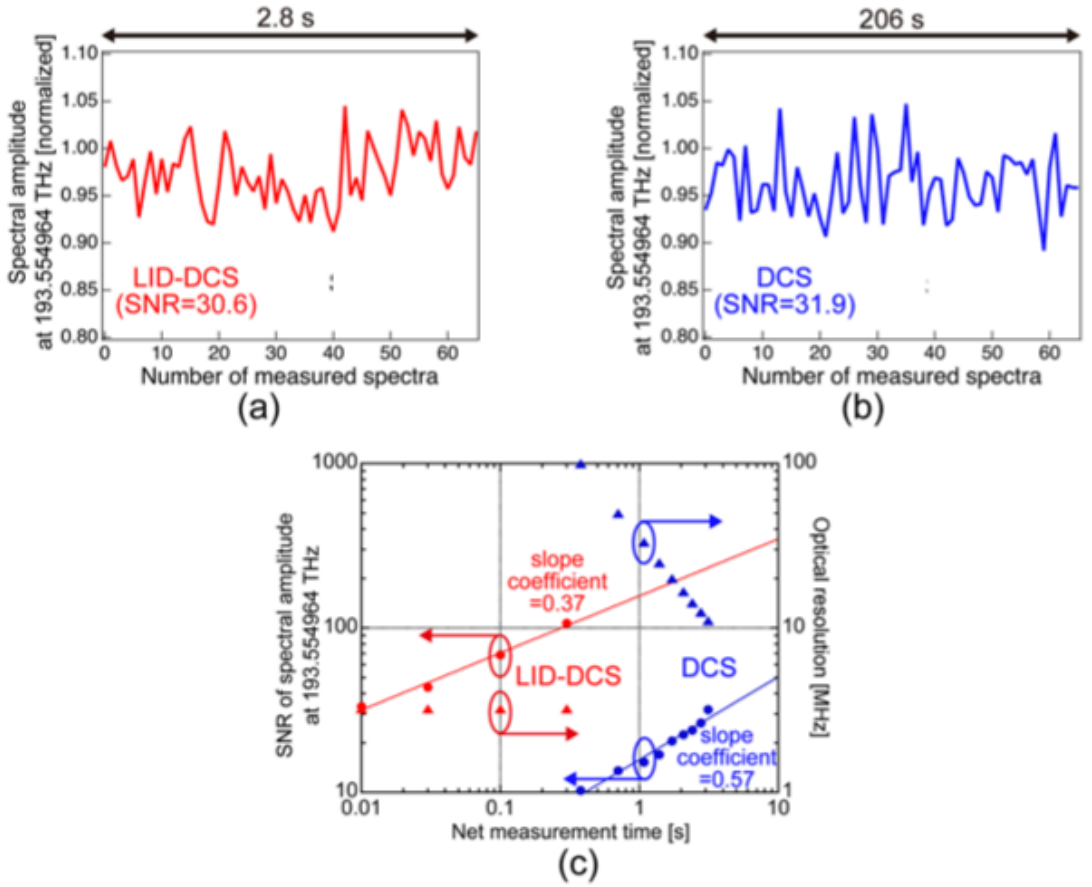

Fig. 2.2. Performance evaluation of LID-DCS and DCS. Fluctuation of spectral amplitude in (a) LID-DCS and (b) DCS. (c) Comparison of SNR of spectral amplitude and optical resolution between LID-DCS and DCS.

2.3.2 Temporal response of LID-DCS and DCS

We next evaluated the temporal response of LID-DCS and DCS when the intensity of the measured signal light was transiently fluctuated. To this end, we chopped the optical beam with a glass

plate (BK7, thickness = 1 mm), leading to a transient change in the optical intensity. Figure 2.3 shows the temporal response of the spectral amplitude at 193.554964 THz for (a) LID-DCS (optical spectral resolution = 1.1 MHz, LID time constant = 30 ms, number of signal accumulation = 1, net acquisition time = 30 ms/spectral_point) and (b) DCS (optical spectral resolution = 100 MHz, number of consecutive interferograms = 1, time window size = 1/frep1 = 10 ns, sampling time interval=21.2 fs, number of temporal data=471,698, number of signal accumulation=6, acquisition time of interferogram = $1/\Delta f_{rep}$ = 4.7 ms/data, FFT calculation time = 0.373 s/data, net acquisition time = 0.401 s/spectrum) with respect to the elapsed time. In this experiment, optical resolution of DCS was 100-times worse than that of LID-DCS to maintain the real-time capability of FFT calculation in DCS by reducing the data size of temporal waveform of the RF interferogram. Nevertheless, the DCS has less discrete sampling points and could not respond to such transient fluctuation sensitively; in contrast, the LID-DCS well responds to the fluctuation by sufficient number of sampling points. Therefore, the LID-DCS will be more powerful than DCS for monitoring of transient signal change, such as gas concentration measurement under air turbulence.

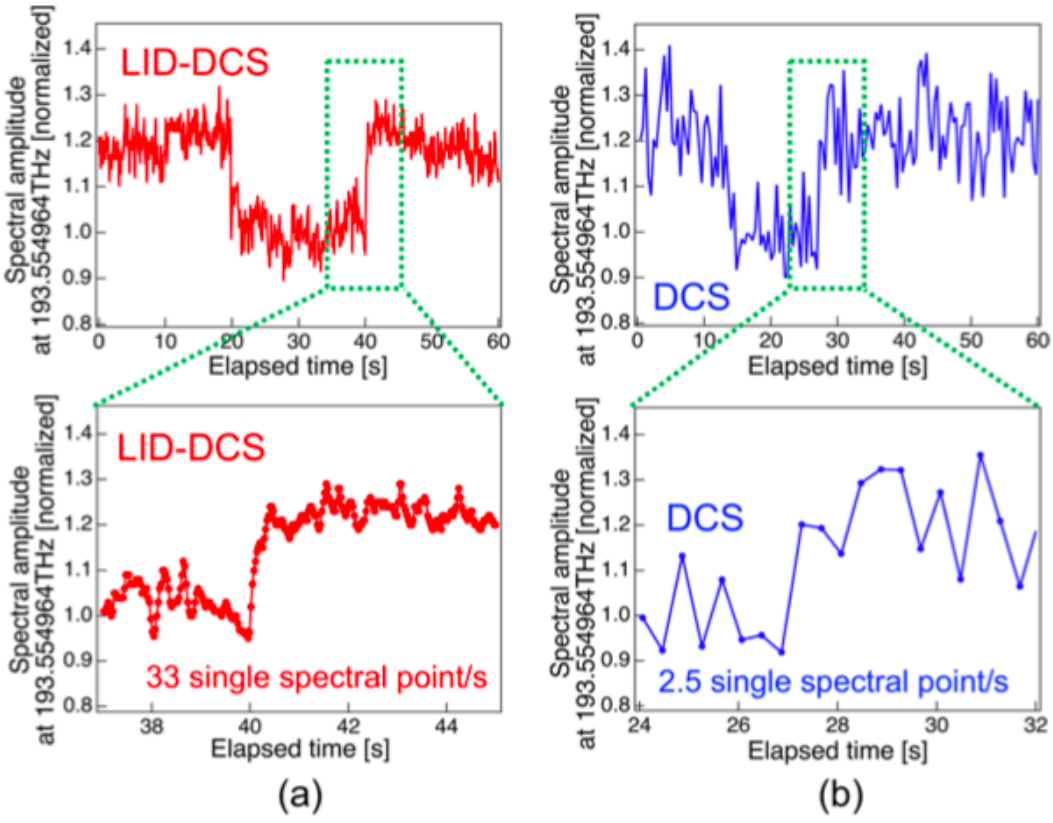

Fig. 2.3. Temporal response of spectral amplitude for (a) LID-DCS and (b) DCS when the optical beam of the signal light was chopped by a glass plate. Lower insets show the magnified temporal response of upper figures.

2.3.3 Spectroscopy of cyanide gas ($H^{13}C^{14}N$)

Finally, we demonstrated spectroscopy of cyanide gas ($H^{13}C^{14}N$) by LID-DCS and DCS. $H^{13}C^{14}N$ gas, contained in a gas cell (cell length = 15 cm , gas pressure = 25 Torr), was placed into an optical path of the signal light. We selected P(9) absorption line of $H^{13}C^{14}N$ gas (center frequency = 193.544907 THz, expected pressure-broadening linewidth = 2.25 GHz) for measurement. Red lines in Fig. 2.4(a) show a mode-resolved amplitude spectrum of OFC within the frequency range from 193.535 THz to 195.555 THz, measured by LID-DCS (optical spectral resolution = 3.24 MHz, LID time constant = 10 ms, number of signal accumulation = 4700, net acquisition time = 47 s/spectral_point). We here extracted 21 RF comb modes at a frequency interval of 1 GHz across the P(9) absorption line by scanning the LID reference-frequency at a frequency interval of 2.12 kHz, leading to the discretely spectral sampling (optical spectral resolution = 3.24 MHz, optical spectral sampling interval = 1 GHz). Since the switching speed of LID frequency is sufficiently fast compared with the LID time constant, the acquisition time for the spectrum is limited by the LID time constant. The total acquisition time was 987 s. Although the net acquisition time was set to be 47 s/spectral_point in this demonstration for high SNR spectrum, there is enough space for further reduction of the acquisition time by reducing the number of signal accumulation. For comparison, we measured the same absorption line by DCS (optical spectral resolution = 10.0 MHz, number of consecutive interferograms = 10, time window size = 100 ns, sampling time interval = 21.2 fs, number of temporal data = 4,716,980, number of signal accumulation = 1000, acquisition time of interferogram = 47 ms/data, FFT calculation time = 3.5 s/data, net acquisition time = 50.5 s/spectrum), as shown in concentrated blue lines of Fig. 2.4(a). We performed a single FFT calculation of the interferogram after the time-domain averaging of interferograms to reduce the number of FFT calculations. Envelopes of amplitude spectrum measured by LID-DCS and DCS were almost overlapped to each other as shown in the difference plot of them. The total acquisition time in LID-DCS was longer that in DCS when monitoring the spectrum itself; however, when monitoring only the single spectral point on the absorption spectral dip for simple gas analysis, the total acquisition time in LID-DCS is 10-times shorter than that in DCS. To determine the center frequency and the linewidth of the measured P(9) absorption line measured by LID-DCS, we performed the curve-fitting analysis using the Voigt function. Red plots and red line in Fig. 2.4(b) show the experimental data of the amplitude spectrum and the corresponding fitting result, respectively. For comparison, literature value of this absorption line position [50] is indicated as a green line in Fig. 2.4(b). The center frequency and the linewidth were determined to be 193.545100 THz and 2.26 GHz. The deviation of them from the expected values might be due to the instability or calibration error of the system used in the DCS, such as frequency counters, sinusoidal function generators, feedback controllers, and so on. However, these results indicate the correct frequency scale and high applicability for gas spectroscopy of LID-DCS.

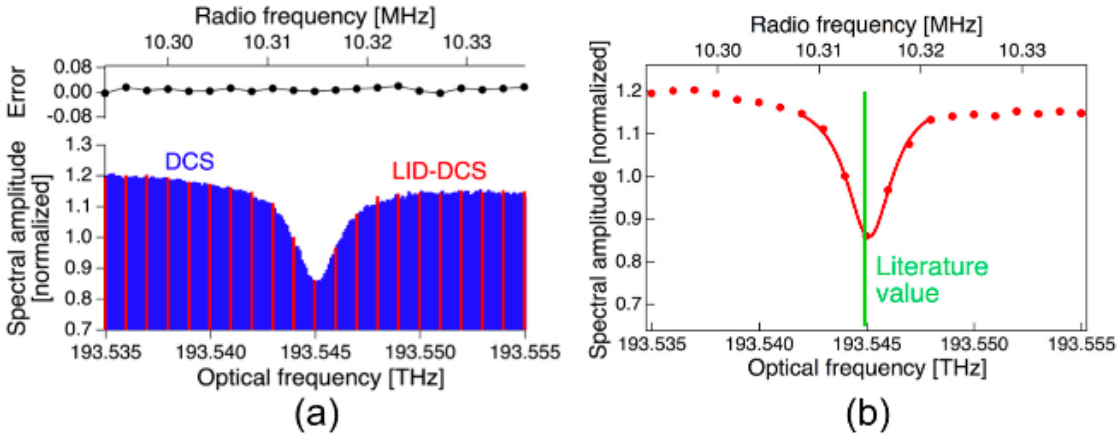

Fig. 2.4. (a) Amplitude spectrum around a P(9) absorption line of cyanide gas ($H^{13}C^{14}N$) measured by LID-DCS (red lines, sampling interval = 1 GHz) and DCS (blue lines, sampling interval = 100 MHz), and its difference plot (upper). (b) Experimental data for the amplitude spectrum (red lines, sampling interval = 1 GHz) and its corresponding curve fitting analysis around the same absorption line. Green line shows a literature value of this absorption line position [50].

2.4. Discussion

One may have doubts about the advantage of LID-DCS compared with usual CW spectroscopy because only a single OFC mode was extracted in this article. CW spectroscopy equipped with tunable CW laser diode [51] benefits from rapid wavelength scanning; however, the spectral resolution and accuracy are respectively limited by optical frequency fluctuation of an unstabilized tunable laser and performance of a wavelength meter. On the other hand, LID-DCS can rapidly select an arbitrary OFC mode within the broadband OFC spectrum, and spectral resolution and accuracy of the selected OFC mode are well secured by phase-locking control of OFC to a frequency standard. Also, one may consider the similarity between LID-DCS and optical vector network analyzer (OVNA) [52], which detects spectral feature of a sample. The spectral resolution and accuracy of OVNA are limited by factors similar to CW spectroscopy. In this way, LID-DCS has the advantage of spectral resolution and accuracy over CW spectroscopy and OVNA although its acquisition speed of spectrum might be sometimes less than that in CW spectroscopy and OVNA.

Simultaneous acquisition of optical amplitude and phase will be another advantage although either the amplitude or phase signal was acquired in this article or the previous article [46,47]. Furthermore, a low frequency electrical noise can be suppressed in the LID-DCS owing to an inherent heterodyne detection mechanism of DCS, while the CW spectroscopy requires an additional intensity or frequency modulator to suppress the low frequency electrical noise. Multi-channel detection is an interesting option for the further extension of LID-DCS although a single-channel LID-DCS was used for gas spectroscopy in this article. The state-of-art multi-channel lock-in detection [47,52,53] will bring

interesting options to LID-DCS. For example, multi-channel LID-DCS enables simultaneous monitoring of different gas samples without the time delay of FFT calculation in DCS. Also, simultaneous monitoring of different absorption lines in the same gas sample makes it possible to determine the gas temperature together with gas concentration [54]. These will be a powerful tool for analysis of combustion process in industry. Work is in progress to investigate multi-channel LID-DCS.

One may consider a possibility to further reduce the FFT calculation time in DCS by devising the data processing. FFT calculation time depends on the FFT calculation algorithm and PC speed. Although full spectrum of amplitude and phase in OFC was obtained by usual FFT calculation algorithm in this article, the specific FFT calculation algorithm suitable to obtain narrow-band spectral data acquisition may enables the further reduction of FFT calculation time in DCS. In this case, one have to compare the speed of electronics in LID-DCS and the speed of PC in DCS. This comparison will be our future work.

3. Dynamic characterization of polarization property in liquid-crystal-on-silicon spatial light modulator using dual-comb spectroscopic polarimetry

3.1. Introduction

Spectroscopic polarimetry (SP) [12-22] is based on simultaneous measurement of polarization and spectrum before and after a broadband light is incident onto a sample. Since change of polarization and spectrum reflects optical property of the sample sensitively, SP is a powerful tool for material characterization in field of fundamental science, industry, and bioscience. For example, spectroscopic ellipsometry [12–21], which is a representative SP with an oblique-incidence reflection configuration, has been applied for evaluation of refractive index and thickness of thin film [12-14], material property such as optical bandgap [15,16] and biosensing of antibody-antigen reaction [17–19].

SP measures broad spectra of a phase difference Δ and an amplitude ratio ψ between two orthogonally linear-polarized lights (x-polarization component and y-polarization component in transmission configuration or p-polarization component and s-polarization component in reflection configuration) when the broadband light with known polarization is incident onto the sample. To obtain these spectra, a spectrum of optical intensity is measured while modulating the polarization of the incident or the output light, and the resulting spectrum is used for determining the spectra of Δ and ψ. Depending on methods of polarization modulation, SP can be classified into three types: rotating-analyzer SP [20], rotating-compensator SP [21], and phase modulation SP [22]. The rotating-analyzer SP and the rotating-compensator SP acquire the spectra of Δ and ψ by a combination of a multi-channel spectrometer with a mechanically rotating polarization optics. Although these SPs have own advantages such as easy implementation and moderate precision, such mechanical polarization modulation limits the mechanical stability and the data acquisition time (typically, several tens of milliseconds) of the SP system. On the other hand, the phase modulation SP benefits from non-mechanical, rapid polarization modulation with a photoelastic modulator (PEM), and hence can reduce the data acquisition time (typically, several tens of microseconds). However, since phase modulation with PEM shows a large dependent on the wavelength and the temperature, the precise compensation of phase modulation is required for SP. Furthermore, the fast modulation speed with PEM (tens of kilohertz) is not so good compatible with the use of a multi-channel spectrometer equipped with a camera (frame rate = 10 ~ 1000 fps). These features make it difficult to apply PEM for broadband SP. In other words, PEM is often used in the monochromatic polarimetry rather than SP.

Recently, DCS [8-11] was applied for spectroscopic ellipsometry without the need for polarization modulation, namely dual-comb spectroscopic ellipsometry or DCSE [23]. In DCSE, ultrahigh-resolution spectra of Δ and ψ is directly obtained from mode-resolved OFC spectra of amplitude and phase for the p-polarization component and s-polarization component of the output light. Such

polarization-modulation-free approach benefits from the immunity to mechanical vibrational noise, thermal instability, and polarization-wavelength dependency, which were often problems in existing mechanical-modulation-based or non-mechanical-modulation-based SP. Effectiveness of DCSE was successfully demonstrated in the determination of thickness in SiO_2 film on Si substrate. On the other hand, there is a considerable need for dynamic monitoring of SiO_2 film process in semiconductor production and antibody-antigen reaction in biosensing. DCSE is one potential candidate for such dynamic monitoring because it has a potential to boost the data acquisition rate up to kilohertz due to its modulation free capability and rapid spectroscopy.

In this topic, for proof of concept in dynamic DCSE, we constructed dual-comb SP with a normal-incidence reflection configuration, we here call it DCSP, and apply it for investigation of dynamic property of a liquid-crystal-on-silicon spatial light modulator.

3.2. Experimental setup

Figure 3.1 shows an experimental setup of DCSP. A pair of mode-locked erbium-doped fiber OFCs (Neoark Co., Japan, OCLS-HSC-D100-TKSM, center wavelength = 1562 nm, spectral bandwidth = 50 nm; signal OFC, f_{ceo1} = 10.5 MHz, f_{rep1} = 100 MHz ; local OFC, f_{ceo2} = 10.5 MHz, f_{rep2} = 99.99895 MHz; $\Delta f_{rep} = f_{rep2} - f_{rep1}$ = 1050 Hz) were used for light sources in DCSP. While f_{ceo1}, f_{rep1}, and f_{ceo2} are phase-locked to a rubidium frequency standard (Rb-FS, Stanford Research Systems, Inc., FS725, frequency = 10 MHz, accuracy = 5×10^{-11}, instability = 2×10^{-11} at 1 s), the local OFC was tightly and coherently locked to the signal OFC with a constant Δf_{rep} using a narrow-linewidth continuous-wave (CW) laser (CWL, Redfern Integrated Optics, Inc., Santa Clara, California, USA, PLANEX, center wavelength = 1550 nm, FWHM < 2.0 kHz) for an intermediate laser via control of f_{rep2} [48,49]. This enables coherent averaging of the interferogram between the signal and local OFCs.

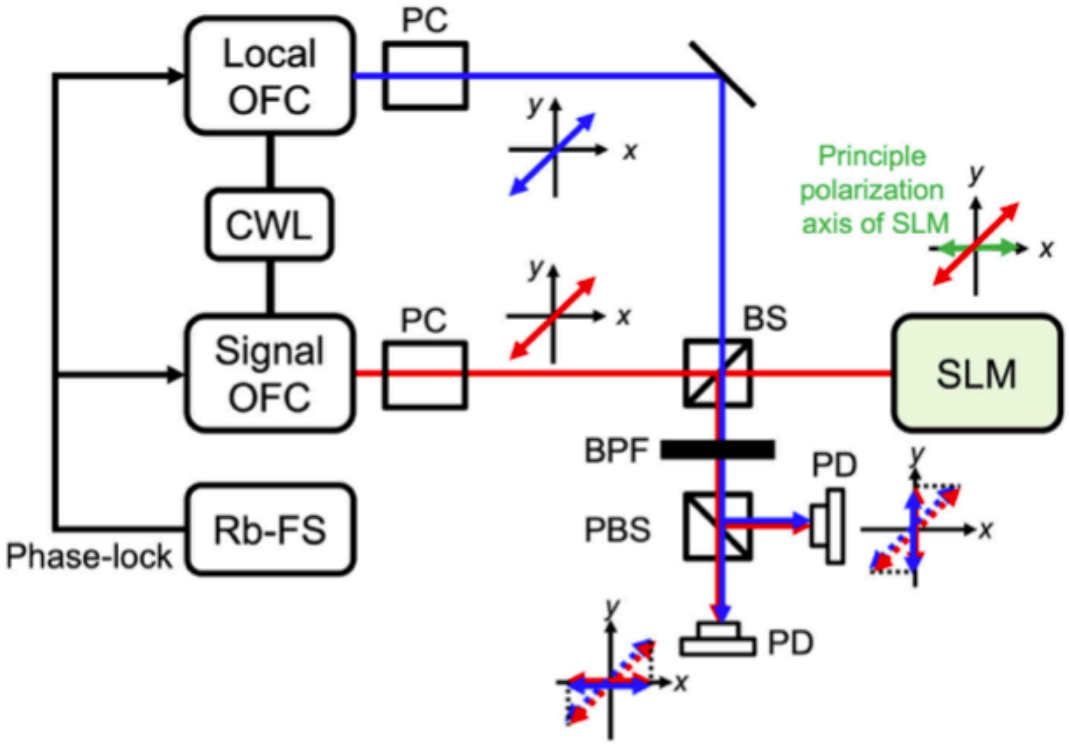

Fig. 3.1. Experimental setup. Signal and local OFCs, signal and local optical frequency combs; CWL, narrow-linewidth CW laser; Rb-FS, rubidium frequency standard; PC, polarization controller; BS, non-polarizing beamsplitter cube; SLM, reflective spatial light modulator; BPF, 1560 ±12 nm band-pass filter; PBS, polarization beam splitter; PDs, photodetectors.

We here define x- and y-polarization components to be horizontally- and vertically-polarized components, respectively. Linear polarization of two OFCs was directed at an angle of +45° to x-polarization component using a polarization controller (PC, extinction ratio = 100,000). After passing through a non-polarizing beamsplitter cube (BS, Thorlabs Inc., Newton, NJ, USA, BS018, split ratio = 50:50), the signal OFC light was incident to a sample perpendicular to its surface. We here used a reflective spatial light modulator based on liquid crystal on silicon (LCOS) technology (SLM, Santec, Komaki, Aichi, Japan, SLM-100, phase stability < 0.002π rad, phase resolution = 10 bit) for a dynamic sample. Principal polarization axis of SLM was set to be parallel to x-polarization component, which tilts by -45° from the polarization angle of OFC1 beam. We confirmed the normal incidence of the signal OFC to the SLM surface by checking the spatial overlapping between the incident light and the reflected light. For more precise analysis, the parameter fitting of the model function for SLM will be useful. After being reflected by the sample, the signal OFC light was spatially overlapped with the local OFC light with +45° linear polarization by BS. This results in generation of the interferogram between the signal and local OFCs. An optical band-pass filter (BPF, Thorlabs Inc., Newton, NJ, USA, FB1560-12, pass band = 1560 ± 12 nm) was used to suppress the aliasing effect in the acquisition of

the interferogram. The x-polarization component and y-polarization component of the generated interferogram was separated by a polarization beam splitter (PBS, Thorlabs Inc., Newton, NJ, USA, PBS104, extinction ratio > 1,000), and then was detected by a pair of photodetectors (PDs, Thorlabs Inc., Newton, NJ, USA, PDA10CF-EC, wavelength = 800-1700 nm, RF bandwidth < 150 MHz). Temporal waveform of the detected electric signal was acquired by a digitizer (National Instruments Corp., Austin, Texas, USA, NI PCI-5122, sampling rate = f_{rep2} = 99,998,950 samples/s, number of sampling points = 95237, resolution = 14 bit). The acquisition rate of interferogram were equal to Δf_{rep}. We acquired consecutive interferograms and integrated them as necessary to obtain appropriate signa-to-noise ratio. Fourier transform of acquired temporal waveforms gives the mode-resolved OFC spectra of amplitude and phase in the x-polarization component and y-polarization component of the interferogram. The resulting spectra were used for calculation of the Δ and ψ spectra of the sample. We beforehand measured an instrumental function of DCSP by using a gold flat mirror as a standard material and calibrated the experimental data of a sample by comparing between them.

3.3. Result

3.3.1. Static characterization of SLM

The SLM used here generates arbitrary 2D phase patterns on a LCOS pixel-by-pixel basis by changing a control parameter for SLM, namely SLM grayscale value. We first investigated the change of Δ and ψ in SLM by DCSP when the SLM grayscale value in the solid image is changed from 0 to 960 step by step at interval of 120. We acquired 1000 temporal waveforms of interferogram (total acquisition time = 952 ms), integrated them, and performed Fourier transform of it. Red pots of Figs. 3.2(a) and 2(b) show 3D plots of Δ and ψ with respect to optical frequency (= 191.5 ~ 192.5 THz, sampling interval = f_{rep1}) and SLM grayscale value (= 0, 120, 240, 360, 480, 600, 720, 840, and 960). For comparison, specification values of SLM for Δ and ψ are indicated as mesh surface. Little dependence of Δ and ψ on optical frequency was confirmed due to flat optical-frequency response of SLM and/or the limited spectral bandwidth of OFC1. On the other hand, the Δ plot shows a linear dependence on the SLM grayscale value while the ψ plot maintains the constant value with respect to the SLM grayscale value (≈ 0.8 rad). Since SLM changes only the optical phase of the x-polarization component to the fixed optical phase of the y-polarization component in the reflected light at this configuration, the behavior of Δ well reflects the polarization modulation by SLM: +45° linearly polarized light for $\Delta = 0$ rad, right-handed circularly polarized light for $\Delta = \pi/2$ rad, +135° linearly polarized light for $\Delta = \pi$ rad, left-handed circularly polarized light for $\Delta = 3\pi/2$ rad, and +225° linearly polarized light for $\Delta = 2\pi$ rad, respectively. The +45° linearly polarized light for $\Delta = 0$ rad is equivalent to the +225° linearly polarized light for $\Delta = 2\pi$ rad although there is a large difference of SLM grayscale value between them. In this way, the SLM could cover the optical phase change over 2π.

To evaluate Δ and ψ in SLM more precisely, we extracted the data of Δ and ψ at 192.000 THz

from Figs. 3.2(a) and 3.2(b) as shown by red plots in Figs. 3.2(c) and 3.2(d). For comparison, we indicate specification values of SLM as blue lines in Figs. 3.2(c) and 3.2(d). The measure values of Δ and ψ were good agreement with the specification value of them. When the measurement accuracy of Δ and ψ (Δ_{RMSE} and ψ_{RMSE}) is defined as a root mean square error (RMSE) between the measured value and the specification value in Δ and ψ, Δ_{RMSE} and ψ_{RMSE} were 1.6×10^{-1} rad and 1.4×10^{-2} rad, respectively. The reason why Δ_{RMSE} is an order of magnitude more than ψ_{RMSE} might be due to polarization dependence of complexed reflectance or transmittance in detection optics such as BS and PBS.

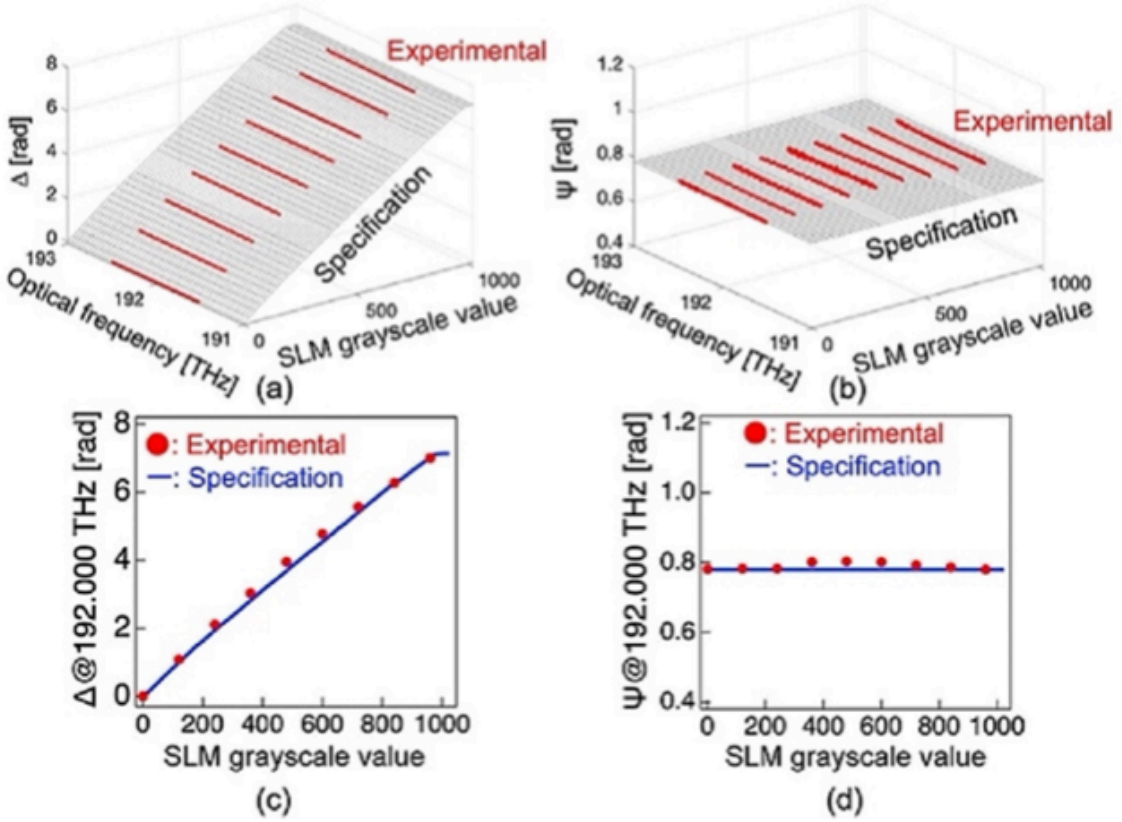

Fig. 3.2. Static characterization of Δ and ψ in SLM. 3D plots of (a) Δ and (b) ψ with respect to optical frequency and SLM grayscale value. (c) Δ and (d) ψ at 192.000 THz with respect to SLM grayscale value.

We next investigated the temporal stability of Δ and ψ in SLM when its SLM grayscale value was set to be a fixed value of 500. We here define the standard deviation of Δ and ψ (Δ_{STD} and ψ_{STD}) as their temporal stability. Red plots in Figs. 3.3(a) and 3.3(b) show Δ_{STD} and ψ_{STD} at 192.000 THz with respect to the accumulation time, respectively. For comparison, we also measured Δ_{STD} and ψ_{STD} at 192.000 THz as indicated by blue plots in Figs. 3.3(a) and 3.3(b) when a gold flat mirror was set as a sample. Δ_{STD} and ψ_{STD} at 192.000 THz was decreased in them when the accumulation time was

increased. Also, Δ_{STD} and ψ_{STD} in SLM was higher than those in the mirror, implying a little instability of Δ and ψ in SLM. ΔSTD at an accumulation time of 1 s for SLM was reasonably coincides with the specification value of phase stability in SLM (< 0.002π rad).

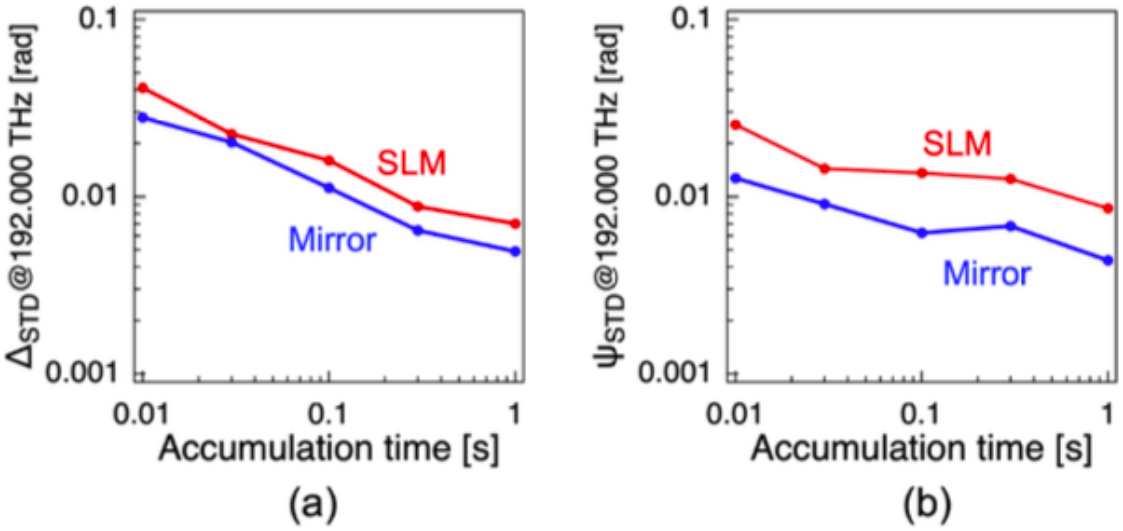

Fig. 3.3. Temporal stability of (a) Δ and (b) ψ with respect to accumulation time in SLM.

3.3.2. Dynamic characterization of SLM

We next investigated characteristics of temporal response in SLM. To this end, we measured the transient change of Δ and ψ in SLM by DCSP when the SLM grayscale level in the solid image was changed as a step function from 0 to 190 which corresponds to change of polarization from a + 45° linearly polarized light to a right-handed circularly polarized light. We acquired 10 temporal waveforms of interferogram (total acquisition time = 9.52 ms), integrated them, and performed Fourier transform of it. Δ and ψ were obtained at a sampling interval of 9.52 ms within a time window size of 3.5 s by repeating the procedure above. Figure 3.4(a) and 3.4(b) shows 3D plots of Δ and ψ with respect to optical frequency and elapsed time. Δ shows similar behavior reflecting a step-function-like change at all optical frequencies while ψ maintained the same level before and after the change of polarization.

To evaluate the temporal dynamics of Δ and ψ in SLM more precisely, we extracted the data of Δ and ψ at 192.000 THz from Figs. 3.4(a) and 3.4(b) as shown by red and blue plots in Fig. 3.4(c). Figure 3.4(d) shows temporally magnified plots of Δ and ψ in the vicinity of a rising edge of Δ in Fig. 3.4(c). Somewhat blunt response of Δ to the step-function-like input was confirmed by a sufficient number of sampling points in DCSP. From Δ and ψ in Fig. 3.4(d), we visualized the dynamic change of polarization before and after the rising edge as plots on the Poincare sphere in Fig. 3.4(e). Here, Poincare parameters (S_0, S_1, S_2, and S_3) are given as follows

$$S_0 = E_x^2 + E_y^2, \quad (1)$$

$$S_1 = E_x^2 - E_y^2, \tag{2}$$

$$S_2 = 2E_xE_ycos\Delta, \tag{3}$$

$$S_3 = 2E_xE_ysin\Delta, \tag{4}$$

where E_x and E_y are x-polarization and y-polarization components of optical electric field. When S_0 is normalized, Eqs. (1) to (4) are transformed as follows

$$S_0 = 1, \tag{5}$$

$$S_1 = \frac{E_x^2 - E_y^2}{E_x^2 + E_y^2} = \frac{1 - tan^2\psi}{1 + tan^2\psi}, \tag{6}$$

$$S_2 = \frac{2E_xE_ycos\Delta}{E_x^2 + E_y^2} = \frac{2tan\psi cos\Delta}{1 + tan^2\psi}, \tag{7}$$

$$S_3 = \frac{2E_xE_ysin\Delta}{E_x^2 + E_y^2} = \frac{2tan\psi sin\Delta}{1 + tan^2\psi}, \tag{8}$$

Plots on the Poincare sphere clearly indicate a straight trajectory from $+S_2$ to $+S_3$, which corresponds to a + 45° linearly polarized light to a right-handed circularly-polarized light. A little deviation from the straight trajectory will be due to the phase stability in DCSP rather than inherent dynamic response of SLM.

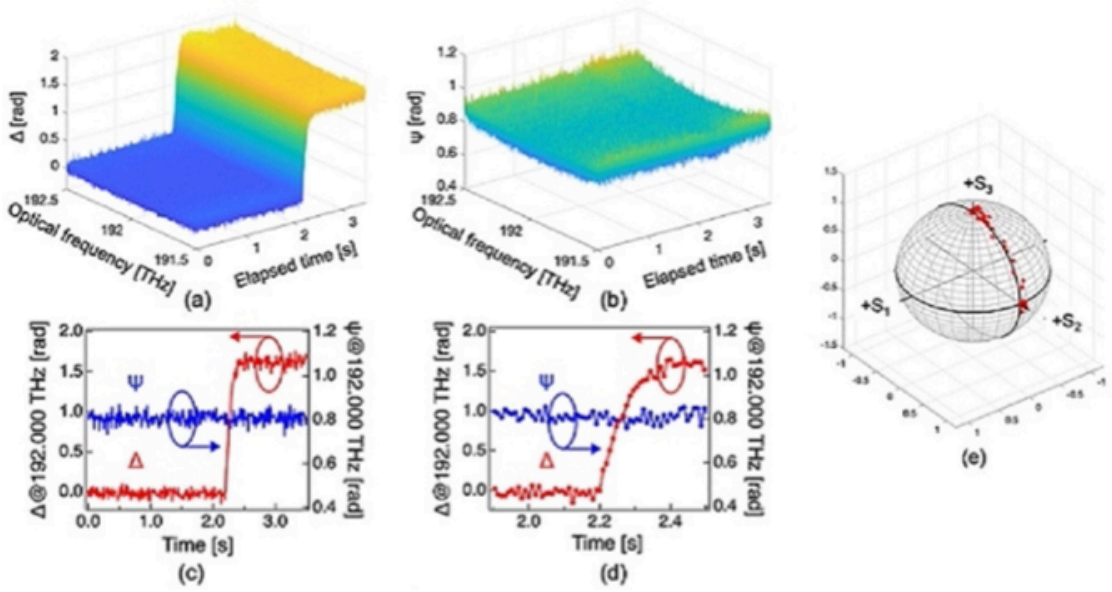

Fig. 3.4. Dynamics characterization of Δ and ψ in SLM. 3D plots of (a) Δ and (b) ψ with respect to optical frequency and elapsed time. Temporal response of Δ and ψ at 192.000 THz within the time range of (c) 0 to 3.5 s and (d) 1.89 s to 2.51 s. (e) Trajectory of polarization change on the Poincare sphere.

We also investigated hysteresis property of dynamic response in SLM by comparing temporal response of Δ and ψ between rising edge and falling edge of a step-function-like polarization change.

Here, the principle polarization axis of the SLM was slightly tilted from *x*-polarization component to change both Δ and ψ by the change of SLM grayscale value. We measured Δ and ψ at a sampling interval of 9.52 ms. Figures 3.5(a) and 3.5(b) respectively show temporally magnified plots of Δ and ψ when the SLM grayscale level in the solid image was increased from 0 to 30. Δ increases while ψ decreases. We determined the time constant of these slopes to be 84 ms for Δ and 82 ms for ψ by the curve fitting analysis with an exponential decay function. It is reasonable that Δ and ψ shows dynamic behavior similar to each other because SLM controls Δ and ψ by changing the alignment direction of liquid crystal molecules with the external electric field. Figures 3.5(c) and 3.5(d) respectively show temporally magnified plots of Δ and ψ when the SLM grayscale level was decreased from 30 to 0. We confirmed the temporal behavior of Δ and ψ opposite to that in Figs. 3.5(a) and 3.5(b). The reason for the opposite trend is due to the tilt angle of the principle polarization axis of the SLM. If the principle polarization axis of the SLM is set to be the opposite direction, the trend of Δ and ψ is coincide with each other. Time constants of these slopes were determined to be 32 ms for Δ and 37 ms for ψ, which are in significant agreement with each other again. More importantly, time constants in Figs. 3.5(a) and 3.5(b) was significantly different from those in Figs. 3.5(c) and 3.5(d). We clearly confirmed the hysteresis property of dynamic response in SLM.

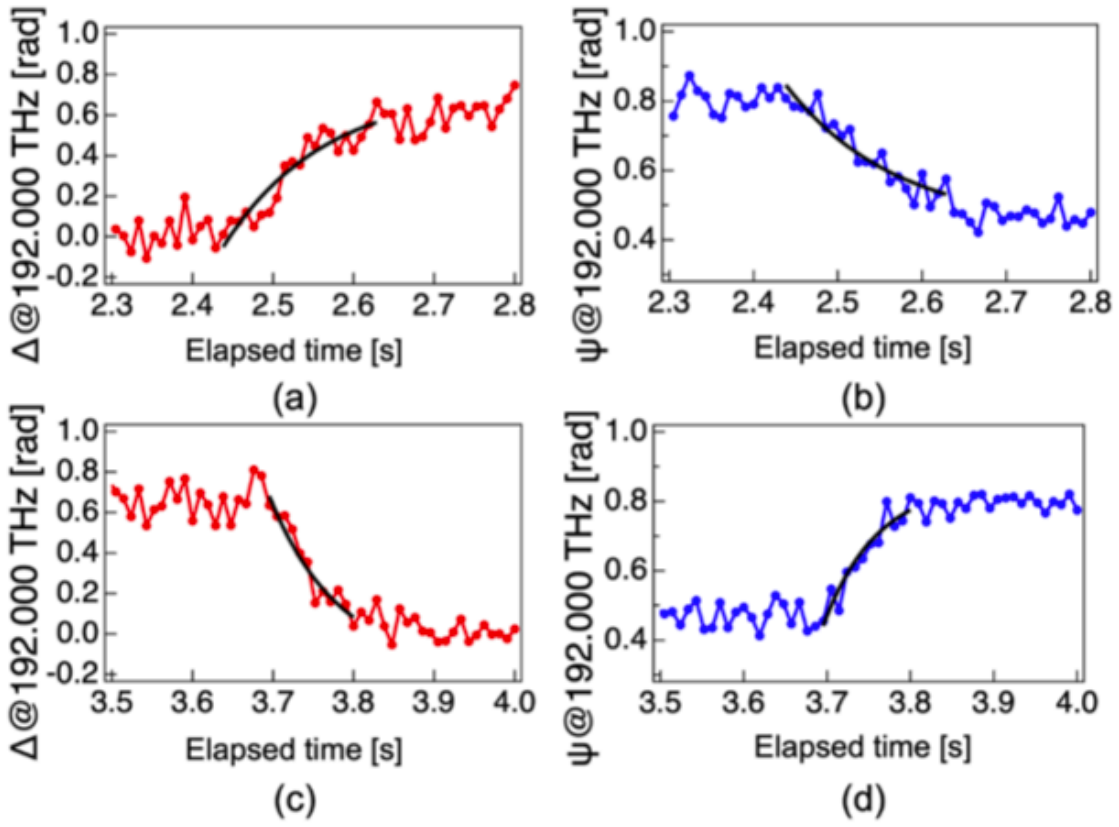

Fig. 3.5. Hysteresis property of dynamic response in SLM. Temporal behavior of (a) Δ and (b) ψ at 192.000 THz when the SLM grayscale level in the solid image was increased as a step function from

0 to 30. Temporal behavior of (c) Δ and (d) ψ at 192.000 THz when the SLM grayscale level was decreased as a step function from 30 to 0.

3.4. Discussion

We discuss the reason for hysteresis property of dynamic response in SLM. Under no external electric field, cylindrical molecules of nematic liquid crystal are oriented in parallel to a surface of SLM and perpendicularly to an incident direction of light beam. When the external electric filed is applied in parallel to the incident direction of light beam, a long axis of liquid-crystalline molecules is aligned along the axis of the external electric filed depending on its field strength. SLM controls the polarization of incident light via the birefringence of liquid-crystalline molecules caused by their aligned direction depending on the applied external electric field. When the external electric field is increased as a step function, liquid-crystalline molecules are transiently affected by both the forced driving force and the inertial restoring force, which are opposite to each other. On the other hand, when the external electric field is decreased as a step function, only the inertial restoring force affects liquid-crystalline molecules. Such difference of contributed force between the step-like-increased and step-like-decreased external electric field leads to hysteresis property of dynamic response in SLM.

We next discuss a possibility to further increase the data acquisition rate Δf_{rep} and broaden the spectral bandwidth $\Delta\nu$ in DCSP. $\Delta\nu$ is related with Δf_{rep} and f_{rep1} as follows

$$\Delta\nu = \frac{f_{rep1}\left(f_{rep1} + \Delta f_{rep}\right)}{2\Delta f_{rep}} \approx \frac{f_{rep1}^2}{2\Delta f_{rep}} \tag{9}$$

For example, in the present setup ($f_{rep1} \approx 100$ MHz, $\Delta f_{rep} \approx 1$ kHz), $\Delta\nu$ is estimated to be 5 THz, corresponding to a wavelength range of 1550 ± 20 nm. In other words, even though OFC has sufficiently broad bandwidth of optical spectrum, the effective spectral bandwidth is limited to avoid the aliasing effect as indicated by Eq. (9). This wavelength range may be still insufficient for some applications of DCSP. From Eq. (9), increase of Δf_{rep} leads to reduction of $\Delta\nu$ whereas $\Delta\nu$ is quadratic of f_{rep1}. Therefore, increase of Δf_{rep} and $\Delta\nu$ can be achieved by increasing both Δf_{rep} and f_{rep1}. Fortunately, increase of f_{rep1}, corresponding to decrease of spectral resolution, is acceptable to DCSP because most of samples in DCSP does not indicate so sharp spectral features. Furthermore, increase of f_{rep1} without the change of total power and spectral bandwidth leads to increase of mode power in OFC and hence increase of signal-to-noise ratio in DCSP, enabling no signal-accumulation measurement at an acquisition rate of Δf_{rep}. There are a few candidates for higher-f_{rep} or GHz-spacing OFCs: electro-optic OFC [55,56], quantum-cascade-laser OFC [57,58], and microcomb [59,60]. Such OFCs were effectively applied for higher-Δf_{rep} DCS [56,58,60] together with nonlinear spectral broadening. For example, in the case of DCSP with f_{rep1} of 10 GHz and Δf_{rep} of 500 kHz, $\Delta\nu$ is increased up to 100 THz, corresponding to a wavelength range of 1550 ± 400 nm. In this way, there is still room for enhancement of the data acquisition rate and the spectral bandwidth by selection of OFCs.

4. Hybrid angular-interrogation surface plasmon resonance sensor based on beam-angle-scanning angular spectrum and beam-angle-fixed reflectance in the near-infrared region for wide dynamic range refractive index sensing

4.1. Introduction

Surface plasmon resonance (SPR) [61,62] is a resonance absorption phenomenon caused by the coupling of an evanescent wave and collective vibrations of free electrons when light is incident on a glass prism coated with the metal thin film around the incident angle of total internal reflection. Because SPR depends on the refractive index (RI) near the sensor surface of the film, it functions as a simple, sensitive, and label-free RI sensor [63,64]. Furthermore, if the sensor surface is modified with an antibody molecular recognition layer, it functions as a biosensor for a target antigen via antibody-to-antigen interaction because such interactions change the effective RI near the sensor surface [65–67].

Because SPR depends on the angle and wavelength of the incident light, SPR sensors are classified into two types: angular interrogation SPR [63,64,68–70] and wavelength interrogation SPR [71,72]. The former acquires the angular spectrum of the SPR dip by measuring the reflectance with respect to the incident angle using monochromatic light. The latter acquires the wavelength spectrum of the SPR dip by measuring the reflectance spectrum using a multichannel spectrometer when broadband light is used for incident light. Although these SPRs have advantages and disadvantages, angular-interrogation SPR is more widely used than wavelength-interrogation SPR owing to its simple and cost-effective setup.

Angular interrogation SPR is further classified into three types: prism-angle-scanning [64,68,69], prism-angle-fixed [67], and multi-channel angle [63,70]. In the prism-angle-scanning type, the angular SPR spectrum is measured by mechanical angle scanning of the prism; however, acquiring the angular SPR spectrum in real time is difficult owing to mechanical scanning. In the prism-angle-fixed type, the SPR reflectance is measured in real time at a fixed incident angle because the RI-dependent shift of the angular SPR spectrum is converted into an RI-dependent change in SPR reflectance at an incident angle close to the linear slope of the SPR dip. However, SPR sensing without acquiring the angular SPR spectrum often causes a temperature drift in the reflected light intensity. In the multi-channel angle type, a line-focused beam of monochromatic light is incident onto the prism as a collimated beam with various incident angles, and a line image of the reflected light from the prism is subsequently acquired using a CCD camera. The angular SPR spectrum is extracted from the obtained image without mechanical scanning of the prism; however, the use of the CCD camera limits the dynamic range of light intensity, and its uneven sensitivity among camera pixels leads to additional background noise in the angular SPR spectrum.

Recently, we reported another angle-scanning type of angular-interrogation SPR based on beam scanning of incident light with a galvanometer mirror (GM) and relay lenses, beam-angle-scanning type [67,73]. GM-based beam angle scanning overcomes slow data acquisition inherent in the prism-angle-scanning type, whereas the use of a photodetector improves the dynamic range of light intensity and eliminates the pixel-to-pixel sensitivity unevenness inherent in the multi-channel angle type.

Herein, we focus on another aspect of the beam-angle scanning type: real-time dual measurement of the angular SPR spectrum and angle-fixed SPR reflectance. If the reflectance at a certain beam angle is extracted from a series of angular SPR spectra continuously acquired by fine, rapid beam scanning, we can acquire a reflectance signal equivalent to that of the angle-fixed type. Simultaneous acquisition of the angular SPR spectrum and angle-fixed SPR reflectance combines a wide RI range of the prism-angle-scanning type and high RI sensitivity of the prism-angle-fixed type, along with the real-time measurement of the multi-channel angle type. In other words, the beam-angle scanning type eliminates the problems of the previous three types and enables the integration of their strengths.

In this study, we further boost the sensing performance of the beam-angle-scanning type by using near-infrared (NIR) light instead of visible light for incident light. This is because the angular SPR dip sharpens in the NIR region more than in the visible region [74]. In the measurement of the angle-fixed SPR reflectance, the sharpening of the angular SPR dip increases the steepness of the SPR dip slope and enhances the RI sensitivity; however, it exhibits the drawback of a reduced measurable range of RI owing to a steep slope. Nonetheless, this drawback can be overcome in the beam-angle-scanning type because the beam-angle-scanning type provides the angular SPR spectrum in addition to the angle-fixed SPR reflectance. We demonstrate the use of NIR light in the beam-angle-scanning type, angular-interrogation SPR to achieve high sensitivity and a wide dynamic range in RI sensing of liquid samples by real-time simultaneous acquisition of angular SPR spectrum and angle-fixed SPR reflectance.

4.2. Principle of operation

We describe the principle of operation for the real-time dual measurement of the angular SPR spectrum and angle-fixed SPR reflectance in the beam-angle-scanning type. Fig. 1(a) shows the spectral behavior of the angular SPR dip with respect to the change in the sample RI. The large change in the sample RI is correctly determined from the spectral shift of the angular SPR dip because the spectral shift is larger than the spectral width of the angular SPR dip. However, in the case of a small RI change, because the SPR spectral shift is smaller than the SPR spectral width, precisely determining the sample RI from the spectral shift of the angular SPR dip is difficult. Therefore, the measurement of the angular SPR spectrum is suitable for wide-range RI measurements but not necessarily for high-precision RI measurements. Furthermore, the measurement of angle-fixed SPR reflectance is suitable for high-precision RI measurements because a small change in sample RI is enhanced by the steep

linear slope of the SPR dip, and the resulting change in reflectance can be precisely measured at a fixed incident angle. However, when the fixed incident angle is out of the steep linear slope of the SPR dip owing to the large change in sample RI, the measurement of angle-fixed SPR reflectance cannot be used for RI sensing. Therefore, although the measurement of angle-fixed SPR reflectance is suitable for high-precision RI measurements, it is unsuitable for wide-range RI measurements. Thus, the measurement of the angular SPR spectrum is complementary to that of the angle-fixed SPR reflectance. The beam-angle scanning type combines the advantages of these two measurements.

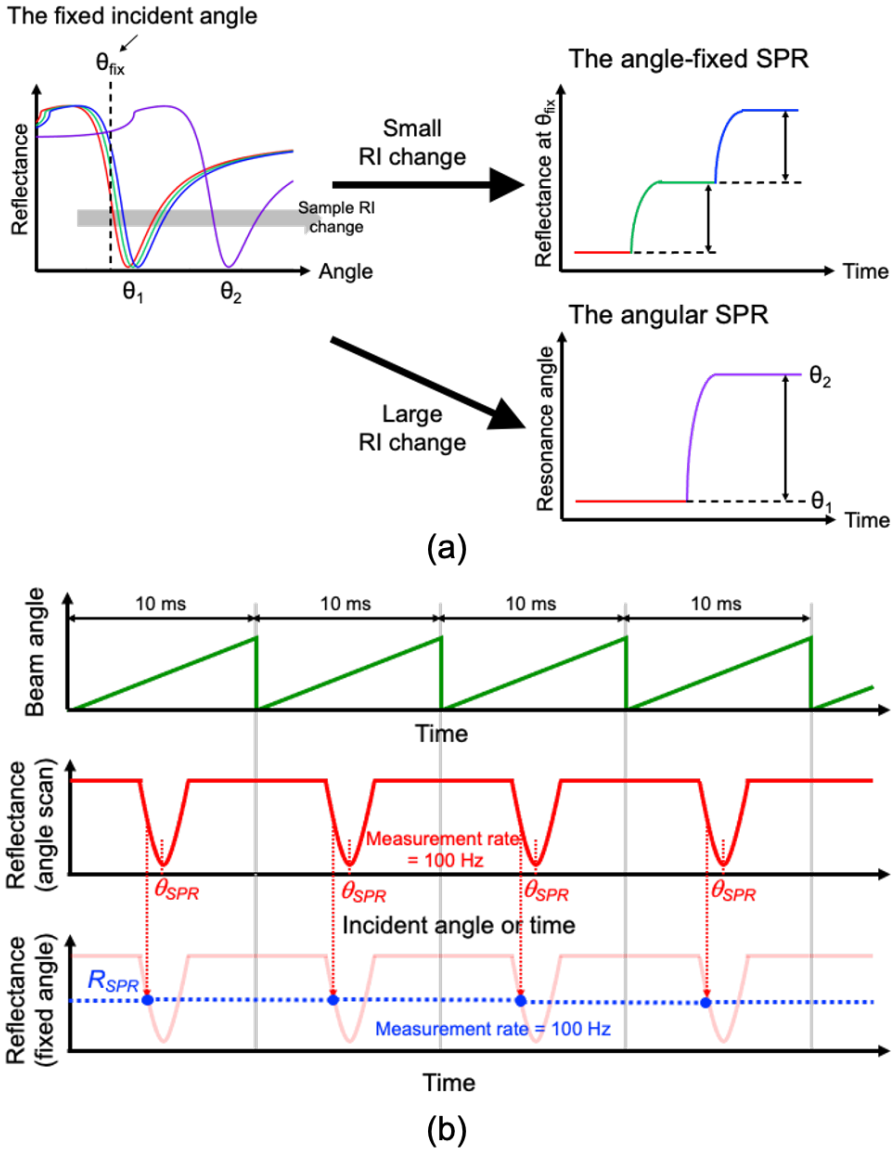

Fig.4.1. The principle of operation for the real-time dual measurement of the angular SPR spectrum and angle-fixed SPR reflectance in the beam-angle-scanning type. (a) the spectral behavior of the angular SPR dip with respect to the change in the sample RI, (b) a measurement timing chart with respect to the beam angle scanning and reflectance.

Fig. 1(b) shows a measurement timing chart with respect to the beam angle scanning and reflectance. The angular SPR spectrum was acquired in synchronization with the beam angle scanning because it corresponds to a temporal change in reflectance with respect to beam angle scanning. The acquisition rate of the angular SPR spectrum increases up to the beam scanning rate (typically, a few hundred hertz) using GM and relay lenses. Furthermore, the use of GM and relay lenses enables fine beam angle scanning in addition to rapid beam angle scanning. In this case, the high reproducibility of beam angle scanning was secured in repetitive reflectance acquisitions. If only the reflectance at a certain beam angle near the SPR dip slope is repetitively extracted from the angular SPR spectrum, the resulting reflectance becomes equivalent to the prism-angle-fixed type sensor signal. The acquisition rate of the angle-fixed reflectance was also equal to the beam scanning rate with the GM. Although the prism-angle-fixed type can acquire both the angular SPR spectrum and angle-fixed SPR reflectance in a similar manner, its acquisition rate is considerably lower than that of the beam-angle-scanning type.

4.3. Experimental setup and sample

Fig. 2 shows a schematic of the experimental setup for hybrid angular-interrogation SPR. We used a single-frequency distributed-feedback (DFB) fiber laser (Koheras BasiK E15, NKT PHOTONICS, Denmark, wavelength = 1550.12 nm, optical power = 40 mW, polarization = linear) for a monochromatic NIR light source. After passing through a Glan–Taylor polarizer (P, GT10-C, Thorlabs Inc., wavelength = 1050–1700 nm, clear aperture = 10 mm, extinction ratio = 100,000:1), the laser beam was angle-scanned within an optical scan angle range of ±1.1° at 100 Hz using a single-axis galvanometer mirror (GM, GVSM001-JP/M, Thorlabs Inc., maximum optical scan angle range = ±20°, resolution = 0.0008°, bandwidth of triangular wave = 175 Hz) and subsequently passed through a pair of relay lenses (RL1, RL2, focal length = 100 mm, diameter = 40 mm). We used the Kretschmann configuration of a right-angle prism for the RI sensing of a liquid sample. A gold (Au) thin film (thickness = 30 nm) was made on the rear surface of a glass right-angle prism (RPB-30-2L, Thorlabs Inc., glass material = BK7, length = 30 mm, uncoated) using a chromium (Cr) thin film (thickness < 5 nm) for the adhesive layer. The laser beam refracted at the incident surface of the prism and moved toward the prism/Cr/Au interface. The combination of GM and relay lenses enables rapid incident-angle scanning of the laser beam (angle range = 61.8–64.0°) near the total reflection angle at a fixed position of the prism/gold interface while maintaining beam collimation (beam diameter = 3.6 mm). The angle-scanning reflection beam was de-scanned using another pair of relay lenses (RL3, RL4, focal length = 100 mm, diameter = 40 mm). The resulting de-scanned beam was detected by a photodetector (PD, PDA20C2, Thorlabs Inc., wavelength = 800–1700 nm, bandwidth = DC ∼5 MHz, active area = 3.14 mm by 3.6 mm). The output voltage signal from the photodetector and the driving voltage signal for the GM were synchronously acquired using a data acquisition board (DAQ, USB-

6361, National Instruments Corp., ADC resolution = 16 bit, maximum sample rate = 2 MSample/s). The resolution and sampling interval of the beam incident on the prism/Cr/Au interface were set to 0.0005° and 0.0022°, respectively. The angular SPR spectrum was obtained at 100 Hz from the signals acquired by the photodetector and GM. Simultaneously, the SPR reflectance was extracted at a fixed incident angle on the angular SPR spectrum, and the angular SPR spectrum was acquired.

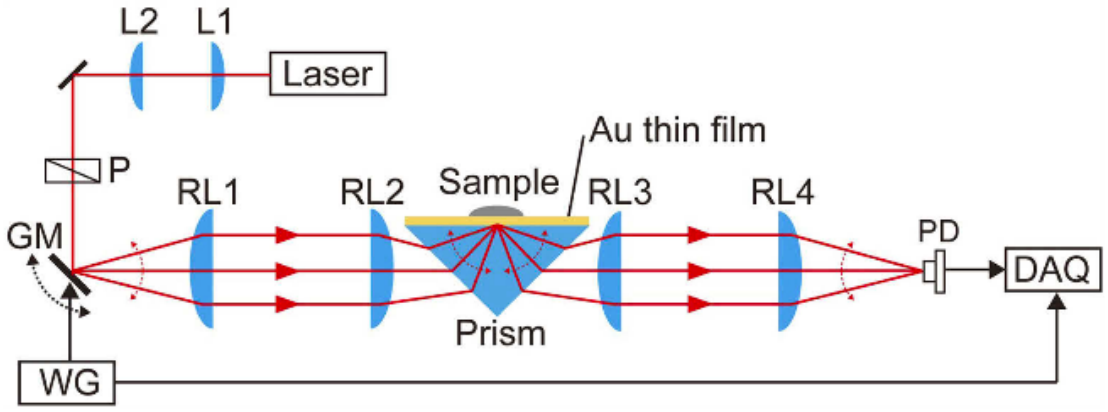

Fig.4.2. A schematic of the experimental setup for hybrid angular-interrogation SPR. Laser, DFB fiber laser; L1 and L2, lenses; P, Glan-Taylor polarizer; GM, single-axis galvanometer mirror; RL1, RL2, RL3, and RL4, relay lenses; PD, photodetector; DAQ, data acquisition board; WG, waveform generator.

4.4. Results

4.4.1. Wide-range RI sensing

For wide-range RI sensing, we used mixtures of ethanol and pure water with different mixture ratios as a sample for RI sensing. The RI of the sample was calculated from the volume ratio of water (RI = 1.3317 refractive index unit or RIU at 1550 nm) and ethanol (RI = 1.3604 RIU at 1550 nm). We prepared five types of samples with different mixture ratios: 0 EtOH% (pure water; RI = 1.3180 RIU), 2.5 EtOH% (RI = 1.3188 RIU), 5 EtOH% (RI = 1.3196 RIU), 7.5 EtOH% (RI = 1.3205 RIU), and 10 EtOH% (RI = 1.3213 RIU).

First, we measured the angular SPR spectra of the water/ethanol samples. Fig. 3(a) shows the angular SPR spectra with respect to different ethanol concentrations (incident angle range = 61.8°–64°). The angular SPR dip appears at approximately 62.5°, indicating its dependence on the ethanol concentration. To determine the center angle θ_{SPR} of the SPR dip, curve fitting analysis with a quintic polynomial function was adopted for the SPR spectra. Fig. 3(b) shows the corresponding sensorgram of θ_{SPR} when the sample RI was increased from 0 EtOH% to 10 EtOH%. The step-like behavior with a constant shift in θ_{SPR} indicates that the angular SPR measurement secures the linearity of the sensor signal in such wide-range RI sensing.

Next, we measured the angle-fixed SPR reflectance of water/ethanol samples. To select a fixed

incident angle, we magnified the angle range of the negative slope of the SPR dip in Fig. 3(a). Fig. 3(c) shows the magnified angular SPR spectra within the incident angle range of 62.2–62.6°. We extracted the SPR reflectance at four different incident angles from the angular SPR spectra: q_1 = 62.300°, q_2 = 62.348°, q_3 = 62.405°, and q_4 = 62.462°. In other words, we extracted the reflectance along the green dashed line for q_1, blue line for q_2, purple line for q_3, and black line for q_4 in Fig. 3(c). Fig. 3(d) shows the corresponding sensorgram of the reflectance R_{SPR} at q_1, q_2, q_3, and q_4 when the sample RI increased from 0 EtOH% to 10 EtOH%. Although the step-like behavior was confirmed depending on the ethanol concentration, the reflectance shift caused by the sample RI change was not even for every incident angle. In this manner, angle-fixed SPR reflectance measurement does not secure the linearity of the sensor signal in wide-range RI sensing. A comparison of the sensor signal linearity between the angular SPR spectrum measurement and angle-fixed SPR reflectance measurements highlights the suitability of the former for wide-range RI sensing.

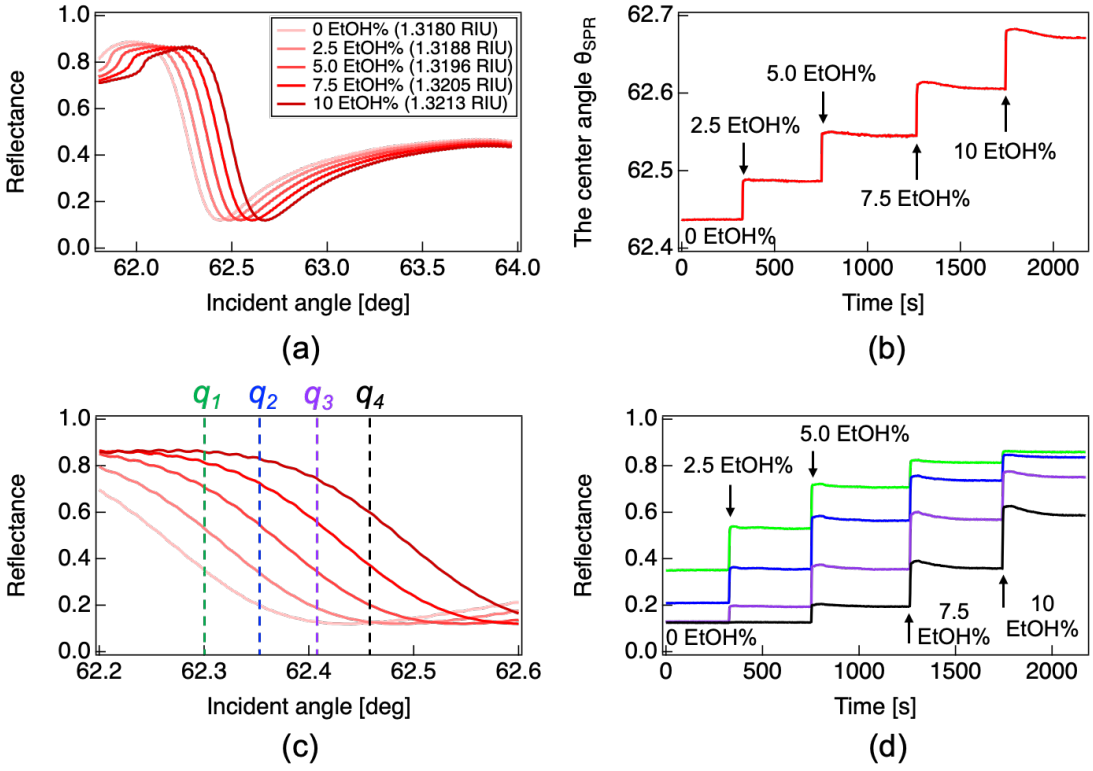

Fig.4.3. (a) The angular SPR spectra with respect to different ethanol concentrations. (b) The sensorgram of θ_{SPR} when the sample RI was increased from 0 EtOH% to 10 EtOH%. (c) The magnified angular SPR spectra within the incident angle range of 62.2–62.6°. (d) The sensorgram of the reflectance R_{SPR} at q_1, q_2, q_3, and q_4 when the sample RI increased from 0 EtOH% to 10 EtOH%.

4.4.2. High-resolution RI sensing

For high-resolution RI sensing, we used more dilute water/ethanol samples: 0 EtOH% (pure water)

sample (RI = 1.3180 RIU), 0.25 EtOH% sample (RI = 1.31808 RIU), 0.50 EtOH% sample (RI = 1.31816 RIU), 0.75 EtOH% sample (RI = 1.31825 RIU), and 1.0 EtOH% sample (RI = 1.31833 RIU). We measured the angle-fixed SPR reflectance of the samples. Fig. 4(a) shows the relationship between the sample RI and R_{SPR} when the incident angle is fixed at 62.274°. A linear relationship was observed between the two variables. From the curve fitting analysis, as shown by the red line in Fig. 4(a), the linear relationship was determined to be R_{SPR} = 239.41RI – 315.09, with a coefficient of determination (R^2) of 0.997. The RI sensitivity was 239.41 1/RIU from the slope coefficient, whereas the RI resolution was estimated to be 2.81 × 10^{-6} RIU from the RI sensitivity and the mean of the standard deviation of the RSPR at each RI. When RI accuracy was defined as the root square mean error (RMSE) between the experimental data and the fitting slope, a value of 2.86 × 10^{-5} RIU was achieved.

For comparison, we also measured the angular SPR spectra of the same water/ethanol samples. Fig. 4(b) shows the relationship between sample RI and θ_{SPR}. We confirmed the linear relationship between them, in which θ_{SPR} = 65.88RI – 24.39, with an R^2 of 0.998. The resulting RI resolution and RI accuracy were determined to be 1.32 ×10^{-5} RIU and 5.22 × 10^{-6} RIU, respectively. A comparison of the RI resolution and RI accuracy between the angle-fixed SPR reflectance measurement and the angular SPR spectrum measurement highlights the superiority of the former for high-resolution RI sensing.

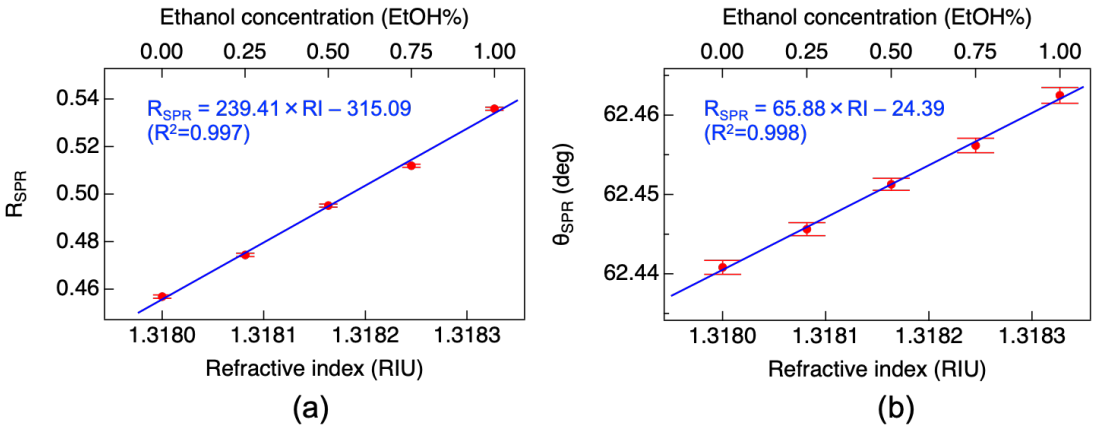

Fig.4.4. (a) The relationship between the sample RI and R_{SPR} when the incident angle is fixed at 62.274°. (b) The relationship between sample RI and θ_{SPR}.

4.5. Discussions

We previously demonstrated a similar GM-based beam-angle-scanning type in the visible-light region for rapid RI sensing and biosensing [73]. Because the previous beam angle scanning is similar to the present one except for the use of monochromatic visible light (wavelength = 633 nm), it has an option for real-time dual measurement of the angular SPR spectrum and angle-fixed SPR reflectance. Herein, we discuss the performance of the hybrid angular-interrogation SPR between the visible and

NIR regions based on theoretical calculations [67].

We first considered the difference in the angular SPR spectrum measurement between the visible and NIR regions. The blue and red lines in Fig. 5(a) show the angular SPR spectra at 633 nm and 1550 nm when pure water is assumed as a sample. Here, the refractive index at 633 nm were assumed to be 1.515 for the prism (BK7), 3.140 + 3.332i for Cr, 0.183 + 3.433i for Au, and 1.3334 for pure water, respectively; thickness was assumed to be 3 nm for Cr and 50 nm for Au, respectively. Similarly, the refractive index at 1550 nm were assumed to be 1.501 for the prism (BK7), 3.668 + 4.180i for Cr, 0.524 + 10.742i for Au, and 1.318 for pure water, respectively; thickness was assumed to be 3 nm for Cr and 30 nm for Au, respectively. The angular SPR dip at 1550 nm was 6 times sharper than that at 633 nm. Furthermore, the RI-dependent shifts of the angular SPR dip at 633 nm and 1550 nm are indicated by the blue and red lines in Fig. 5(b). The linear slope at 1550 nm was 1.7 times steeper than that at 633 nm. In other words, such a less steep slope is useful for wide-range RI sensing within the limited angle range of GM-based beam scanning. Because the RI precision depends on the ratio of the RI-dependent shift to the SPR dip width, we defined the ratio as the figure of merit (FOM) in angular-interrogation SPR. The blue and red lines in Fig. 5(c) show the FOM with respect to the sample RI at 633 nm and 1550 nm, respectively. The RI-dependent FOM shift at 1550 nm is 7 times larger than that at 633 nm. Thus, NIR angular-interrogation SPR has the advantage of wide-range and high-precision RI sensing over visible angular-interrogation SPR.

Next, we considered angle-fixed SPR reflectance measurement. The RI-dependent SPR reflectance at a fixed incident angle also depends on both the SPR dip width [see Fig. 5(a)] and the RI-dependent SPR dip shift. The blue and red lines in Fig. 5(d) show the RI-dependent reflectance shifts at 633 and 1550 nm, respectively. The RI-dependent SPR reflectance shift at 1550 nm is eight times larger than that at 633 nm. In other words, such a large reflectance shift is effective for high-resolution RI sensing. Thus, the hybrid angular-interrogation SPR in the NIR region benefits from a wide range, high precision, and high resolution compared with the hybrid angular-interrogation SPR in the visible region.

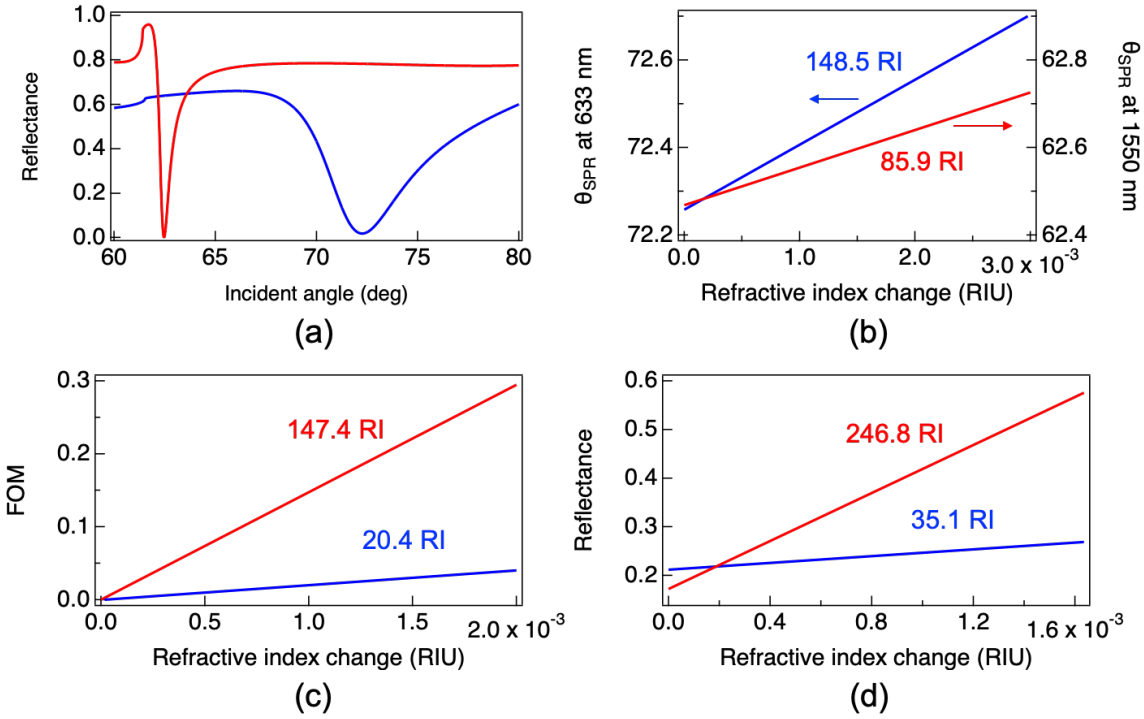

Fig.4.5. The blue and red lines shows (a) The angular SPR spectra when pure water is assumed as a sample, (b) the RI-dependent shifts of the angular SPR dip, (c) The FOM with respect to the sample RI and (d) The RI-dependent reflectance shifts, at 633 nm and 1550 nm, respectively.

5. Conclusion

In this PhD thesis, we introduce NIR light such as OFC and CW light to enhance the performance of three kinds of optical measurements: gas spectroscopy, spectroscopic polarimetry, and surface plasmon resonance sensor. To perform the proof of concept in those optical measurements, the following three topics were investigated in this PhD thesis.

(1). Lock-in-detection dual-comb spectroscopy [1]

(2). dynamic characterization of polarization property in liquid-crystal-on-silicon spatial light modulator using dual-comb spectroscopic polarimetry [2]

(3). Hybrid angular-interrogation surface plasmon resonance sensor based on beam-angle-scanning angular spectrum and beam-angle-fixed reflectance in the near-infrared region for wide dynamic range refractive index sensing [3, 4]

In the first topic of this PhD thesis, we demonstrated use of LID in DCS. This combination, LID-DCS, has potential to largely reduce the time spent for FFT calculation of a huge amount of temporal data because it depends on the frequency-domain measurement without the need for FFT calculation. The advantage of LID-DCS over DCS was highlighted in the rapid data acquisition under the condition of monochromatic spectral analysis due to no FFT calculation. Although the large amount of spectral data points available in the usual DCS are sometimes useful because of such as the application of spectral fitting to improve the accuracy of gas spectroscopy, LID-DCS benefits from the faster temporal response than usual DCS while maintaining the high resolution and accuracy comparable to usual DCS. Such characteristics of LID-DCS will be a powerful tool for monitoring of transient signal change, such as gas concentration measurement under air turbulence. Furthermore, options for multi-channel detection or imaging will expand the application fields of LID-DCS.

In the second topic of this PhD thesis, we demonstrated the dynamic characterization of polarization property in LCOS-SLM by DCSP. The proposed DCSP system has a potential to boost the scan rate of Δ and ψ spectra measurement up to 1050 Hz due to the direct polarization determination without the need for polarization modulation benefitting from DCS-based polarimetry. Effectiveness of DCSP was highlighted by visualizing the hysteresis property of dynamic response in SLM at a sampling rate of 105 Hz, indicating the dynamic interaction between the forced driving force and the inertial restoring force in liquid-crystalline molecules of SLM. Although the achieved data acquisition rate and the spectral bandwidth in this article may be still insufficient for some applications of dynamic SP, DCSP has a sufficient room to further boost the data acquisition rate and broaden the spectral bandwidth by use of GHz-spacing OFCs. DCSP will be a powerful tool for dynamic characterization of various samples.

In the third topic of this PhD thesis, Simultaneous measurement of the angular SPR spectrum and

angle-fixed SPR reflectance in the NIR region was demonstrated at 100 Hz through rapid, high-precision beam angle scanning based on a combination of GM and relay lenses. Wide-range RI sensing of water/ethanol solutions was performed within an RI range of 1.3180–1.3213 RIU by angular SPR spectrum measurements. Although the range of the incident angle was set between 61.8° and 64° by an optical scan angle range of ±1.1° in GM, it could be further expanded by the complete utilization of the maximum optical scan angle range of GM (= ±20°) and/or modification of the relay-lens configuration while maintaining the same measurement rate, thereby boosting the wide-range RI sensing. Furthermore, the angle-fixed reflectance measurement achieved an RI resolution of 2.81×10^{-6} RIU and an RI accuracy of 2.86×10^{-5} RIU in the RI sensing of water/ethanol solutions, highlighting the high-precision RI sensing performance. Furthermore, the superiority of the combination of hybrid angular-interrogation SPR and NIR light was proven by comparison using visible light. The proposed hybrid angular-interrogation SPR is a powerful tool for wide-dynamic-range RI sensing and biosensing.

Those three topics of this PhD thesis highlighted performance in gas spectroscopy, spectroscopic polarimetry, and surface plasmon resonance sensor was boosted by use of novel characteristics in NIR light. These NIR-light-based optical measurements will expand their scope into industrial and biomedical applications.

Reference

1. H. Koresawa, K. Shibuya, T. Minamikawa, A. Asahara, R. Oe, T. Mizuno, M. Yamagiwa, Y. Mizutani, T. Iwata, H. Yamamoto, K. Minoshima, and T. Yasui, "Lock-in-detection dual-comb spectroscopy," OSA Continuum **2**(6), 1998–2007 (2019).
2. H. Koresawa, M. Gourayeb, K. Shibuya, T. Mizuno, E. Hase, Y. Tokizane, R. Oe, T. Minamikawa, and T. Yasui, "Dynamic characterization of polarization property in liquid-crystal-on-silicon spatial light modulation using dual-comb spectroscopic polarimetry", Opt. Express **28**(16), 23584-23593 (2020).
3. H. Koresawa, K. Seki, E. Hase, Y. Tokizane, T. Minamikawa, T. Yano, T. Kajisa, and T. Yasui, "Beam-angle-scanning surface plasmon resonance sensor for rapid, high-precision sensing of refractive index and bio-molecules", Opt. Continuum **1**(3), 565-574 (2022).
4. H. Koresawa, K. Seki, I. Tsushima, K. Kamada, E. Hase, Y. Tokizane, T. Minamikawa, T. Yano, T. Kajisa, and T. Yasui, "High dynamic range refractive index sensing by beam-angle-scanning surface plasmon resonance sensor using NIR light source", *in the process of writing*.
5. T. Udem, J. Reichert, R. Holzwarth, and T. W. Hänsch, "Accurate measurement of large optical frequency differences with a mode-locked laser," Opt. Lett. **24**(13), 881–883 (1999).
6. M. Niering, R. Holzwarth, J. Reichert, P. Pokasov, T. Udem, M. Weitz, T. W. Hänsch, P. Lemonde, G. Santarelli, M. Abgrall, P. Laurent, C. Salomon, and A. Clairon, "Measurement of the hydrogen 1S-2S transition frequency by phase coherent comparison with a microwave cesium fountain clock," Phys. Rev. Lett. **84(**24), 5496–5499 (2000).
7. T. Udem, R. Holzwarth, and T. W. Hänsch, "Optical frequency metrology," Nature **416**(6877), 233–237 (2002).
8. S. Schiller, "Spectrometry with frequency combs," Opt. Lett. **27**(9), 766–768 (2002).
9. F. Keilmann, C. Gohle, and R. Holzwarth, "Time-domain mid-infrared frequency-comb spectrometer," Opt. Lett. **29**(13), 1542–1544 (2004).
10. T. Yasui, Y. Kabetani, E. Saneyoshi, S. Yokoyama, and T. Araki, "Terahertz frequency comb by multifrequency-heterodyning photoconductive detection for high-accuracy, high-resolution terahertz spectroscopy," Appl. Phys. Lett. **88**(24), 241104 (2006).
11. I. Coddington, N. Newbury, and W. Swann, "Dual-comb spectroscopy," Optica **3**(4), 414–426 (2016).
12. P. Löper, M. Stuckelberger, B. Niesen, J. Werner, M. Filipič, S. J. Moon, J. H. Yum, M. Topič, S. D. Wolf, and C. Ballif, "Complex refractive index spectra of CH3NH3PbI3 perovskite thin films determined by spectroscopic ellipsometry and spectrophotometry," J. Phys. Chem. Lett. **6**(1), 66–71 (2015).

13. C. Yim, M. O'Brien, N. McEvoy, S. Winters, I. Mirza, J. G. Lunney, and G. S. Duesberg, "Investigation of the optical properties of MoS2 thin films using spectroscopic ellipsometry," Appl. Phys. Lett. **104**(10), 103114 (2014).
14. F. L. McCrackin, E. Passaglia, R. R. Stromberg, and H. L. Steinberg, "Measurement of the thickness and refractive index of very thin films and the optical properties of surfaces by ellipsometry," J. Res. Natl. Bur. Stand., Sect. A **67A**(4), 363–377 (1963).
15. S. G. Lim, S. Kriventsov, and T. N. Jackson, "Dielectric functions and optical bandgaps of high-K dielectrics for metal-oxide-semiconductor field-effect transistors by far ultraviolet spectroscopic ellipsometry," J. Appl. Phys. **91**(7), 4500–4505 (2002).
16. H. L. Liu, C. C. Shen, S. H. Su, C. L. Hsu, M. Y. Li, and L. J. Li, "Optical properties of monolayer transition metal dichalcogenides probed by spectroscopic ellipsometry," Appl. Phys. Lett. **105**(20), 201905 (2014).
17. H. Arwin, "Is ellipsometry suitable for sensor applications?" Sens. Actuators, A **92**(1-3), 43–51 (2001).
18. K. Spaeth, A. Brecht, and G. Gauglitz, "Studies on the biotin-avidin multilayer adsorption by spectroscopic ellipsometry," J. Colloid Interface Sci. **196**(2), 128–135 (1997).
19. Z. H. Wang and G. Jin, "A label-free multisensing immunosensor based on imaging ellipsometry," Anal. Chem. **75**(22), 6119–6123 (2003).
20. D. E. Aspnes, "Fourier transform detection system for rotating-analyzer ellipsometers," Opt. Commun. **8**(3), 222–225 (1973).
21. P. S. Hauge and F. H. Dill, "A rotating-compensator Fourier ellipsometer," Opt. Commun. **14**(4), 431–437 (1975).
22. C. Y. Han and Y. F. Chao, "Photoelastic modulated imaging ellipsometry by stroboscopic illumination technique," Rev. Sci. Instrum. **77**(2), 023107 (2006).
23. T. Minamikawa, Y. Hsieh, K. Shibuya, E. Hase, Y. Kaneoka, S. Okubo, H. Inaba, Y. Mizutani, H. Yamamoto, T. Iwata, and T. Yasui, "Dual-comb spectroscopic ellipsometry," Nat. Commun. **8**(1), 610 (2017).
24. P. Pattnaik, "Surface plasmon resonance," Appl. Biochem. Biotechnol. 126(2), 079–092 (2005).
25. J. Homola, S. S. Yee, and G. Gauglitz, "Surface plasmon resonance sensors," Sens. Actuators, B **54**(1-2), 3–15 (1999).
26. J. Homola, "Present and future of surface plasmon resonance biosensors," Anal. Bioanal. Chem. **377**(3), 528–539 (2003).
27. E. Wijaya, C. Lenaerts, S. Maricot, J. Hastanin, S. Habraken, J.-P. Vilcot, R. Boukherroub, and S. Szunerits, "Surface plasmon resonance-based biosensors: From the development of different SPR structures to novel surface functionalization strategies," Curr. Opin. Solid State Mater. Sci. **15**(5), 208–224 (2011).

28. K. Matsubara, S. Kawata, and S. Minami, “Optical chemical sensor based on surface plasmon measurement,” Appl. Opt. **27**(6), 1160–1163 (1988).
29. W. Y. W. Yusmawati, H. P. Chuah, and M. Y. W. Mahmood, “Optical properties and sugar content determination of commercial carbonated drinks using surface plasmon resonance,” Am. J. Appl. Sci. **4**(1), 1–4 (2007).
30. H. Liang, H. Miranto, N. Granqvist, J. W. Sadowski, T. Viitala, B. Wang, and M. Yliperttula, “Surface plasmon resonance instrument as a refractometer for liquids and ultrathin films,” Sens. Actuators, B **149**(1), 212–220 (2010).
31. K. Tiwari and S. C. Sharma, “Surface plasmon based sensor with order-of-magnitude higher sensitivity to electric field induced changes in dielectric environment at metal/nematic liquid-crystal interface,” Sens. Actuators, A **216**, 128–135 (2014).
32. C. E. H. Berger, T. A. M. Beumer, R. P. H. Kooyman, and J. Greve, “Surface plasmon resonance multisensing,” Anal. Chem. **70**(4), 703–706 (1998).
33. R. Ziblat, V. Lirtsman, D. Davidov, and B. Aroeti, “Infrared surface plasmon resonance: a novel tool for real time sensing of variations in living cells,” Biophys. J. **90**(7), 2592–2599 (2006).
34. A. Shalabney and I. Abdulhalim, “Figure-of-merit enhancement of surface plasmon resonance sensors in the spectral interrogation,” Opt. Lett. **37**(7), 1175–1177 (2012).
35. S. Zeng, D. Baillargeat, H.-P. Ho, and K.-T. Yong, “Nanomaterials enhanced surface plasmon resonance for biological and chemical sensing applications,” Chem. Soc. Rev. **43**(10), 3426–3452 (2014).
36. Y. Zhao, S. Gan, G. Zhang, and X. Dai, “High sensitivity refractive index sensor based on surface plasmon resonance with topological insulator,” Results Phys. **14**, 102477 (2019).
37. D. Lakayan, J. Tuppurainen, M. Albers, M. J. van Lint, D. J. van Iperen, J. J. A. Weda, J. Kuncova-Kallio, G. W. Somsen, and J. Kool, “Angular scanning and variable wavelength surface plasmon resonance allowing free sensor surface selection for optimum material- and bio-sensing,” Sens. Actuators, B **259**, 972–979 (2018).
38. D. Wang, F.-C. Loo, H. Cong, W. Lin, S. K. Kong, Y. Yam, S.-C. Chen, and H. P. Ho, “Real-time multi-channel SPR sensing based on DMD-enabled angular interrogation,” Opt. Express **26**(19), 24627–24636 (2018).
39. S. Okubo, K. Iwakuni, H. Inaba, K. Hosaka, A. Onae, H. Sasada, and F. L. Hong, “Ultra-broadband dual-comb spectroscopy across 1.0–1.9μm,” Appl. Phys. Express **8**(8), 082402 (2015).
40. G. B. Rieker, F. R. Giorgetta, W. C. Swann, J. Kofler, A. M. Zolot, L. C. Sinclair, E. Baumann, C. Cromer, G. Petron, C. Sweeney, P. P. Tans, I. Coddington, and N. R. Newbury, “Frequency-comb-based remote sensing of green gases over kilometer air paths,” Optica **1**(5), 290–298 (2014).

41. K. C. Cossel, E. M. Waxman, F. R. Giorgetta, M. Cermak, I. R. Coddington, D. Hesselius, S. Ruben, W. C. Swann, G.-W. Truong, G. B. Rieker, and N. R. Newbury, "Open-path dual-comb spectroscopy to an airborne retroreflector," Optica **4**(7), 724–728 (2017).
42. P. J. Schroeder, R. J. Wright, S. Coburn, B. Sodergren, K. C. Cossel, S. Droste, G. W. Truong, E. Baumann, F. R. Giorgetta, I. Coddington, N. R. Newbury, and G. B. Rieker, "Dual frequency comb laser absorption spectroscopy in a 16 MW gas turbine exhaust," Proc. Combust. Inst. **36**(3), 4565–4573 (2017).
43. B. Berinhardt, E. Sorokin, P. Jacquet, R. Thon, T. Becker, I. T. Sorokina, N. Picque, and T. W. Hänsch, "Mid-infrared dual-comb spectroscopy with 2.4 μm Cr2+ :ZnSe femtosecond lasers," Appl. Phys. B: Lasers Opt. **100**(1), 3–8 (2010).
44. T. Yasui, Y. Kabetani, E. Saneyoshi, S. Yokoyama, and T. Araki, "Terahertz frequency comb by multi-frequency-heterodyning photoconductive detection for high-accuracy, high-resolution terahertz spectroscopy," Appl. Phys. Lett. **88**(24), 241104 (2006).
45. Y. D. Hsieh, Y. Iyonaga, Y. Sakaguchi, S. Yokoyama, H. Inaba, K. Minoshima, F. Hindle, T. Araki, and T. Yasui, "Spectrally interleaved, comb-mode-resolved spectroscopy using swept dual terahertz combs," Sci. Rep. **4**(1), 3816 (2015).
46. S. Yokoyama, T. Yokoyama, Y. Hagihara, T. Araki, and T. Yasui, "A distance meter using a terahertz intermode beat in an optical frequency comb," Opt. Express **17**(20), 17324–17333 (2009).
47. R. Yang, F. Pollinge, K. Meiners-Hagen, M. Krystek, J. Tan, and H. Bosse, "Absolute distance measurement by dual-comb interferometry with multi-channel digital lock-in phase detection," Meas. Sci. Technol. **26**(8), 084001 (2015).
48. A. Asahara, A. Nishiyama, S. Yoshida, K. Kondo, Y. Nakajima, and K. Minoshima, "Dual-comb spectroscopy for rapid characterization of complex optical properties of solids," Opt. Lett. **41**(21), 4971–4974 (2016).
49. K. Shibuya, T. Minamikawa, Y. Mizutani, H. Yamamoto, K. Minoshima, T. Yasui, and T. Iwata, "Scan-less hyperspectral dual-comb single-pixel-imaging in both amplitude and phase," Opt. Express **25**(18), 21947–21957 (2017).
50. W. C. Swann and S. L. Gilbert, "Line centers, pressure shift, and pressure broadening of 1530-1560 nm hydrogen cyanide wavelength calibration lines," J. Opt. Soc. Am. B **22**(8), 1749–1756 (2005).
51. Z. Tang, S. Pan, and J. Yao, "A high resolution optical vector network analyzer based on a wideband and wavelength-tunable optical single-sideband modulator," Opt. Express **20**(6), 6555–6560 (2012).

52. N. Ishii, E. Tokunaga, S. Adachi, T. Kimura, H. Matsuda, and T. Kobayashi, “Optical frequency- and vibrational time- resolved two-dimensional spectroscopy by real-time impulsive resonant coherent Raman scattering in polydiacetylene,” Phys. Rev. A **70**(2), 023811 (2004).
53. P. Mao, Z. Wang, W. Dang, and Y. Wenga, “Multi-channel lock-in amplifier assisted femtosecond time-resolved fluorescence non-collinear optical parametric amplification spectroscopy with efficient rejection of superfluorescence background,” Rev. Sci. Instrum. **86**(12), 123113 (2015).
54. Y. Deguchi, M. Noda, Y. Fukuda, Y. Ichinose, Y. Endo, M. Inada, Y. Abe, and S. Iwasaki, “Industrial applications of temperature and species concentration monitoring using laser diagnostics,” Meas. Sci. Technol. **13**(10), R103–R115 (2002).
55. T. Kawanishi, T. Sakamoto, S. Shinada, and M. Izutsu, “Optical frequency comb generator using optical fiber loops with single-sideband modulation,” IEICE Electron. Express **1**(8), 217–221 (2004).
56. M. M. Pedro, B. Jerez, and P. Acedo, “Dual electro-optic optical frequency combs for multiheterodyne molecular dispersion spectroscopy,” Opt. Express **23**(16), 21149–21158 (2015).
57. A. Hugi, G. Villares, S. Blaser, H. C. Liu, and J. Faist, “Mid-infrared frequency comb based on a quantum cascade laser,” Nature **492**(7428), 229–233 (2012).
58. G. Villares, A. Hugi, S. Blaser, and J. Faist, “Dual-comb spectroscopy based on quantum-cascade-laser frequency combs,” Nat. Commun. **5**(1), 5192 (2014).
59. P. Del’Haye, A. Schliesser, O. Arcizet, T. Wilken, R. Holzwarth, and T. J. Kippenberg, “Optical frequency comb generation from a monolithic microresonator,” Nature **450**(7173), 1214–1217 (2007).
60. M. G. Suh, Q. F. Yang, K. Y. Yang, X. Yi, and K. J. Vahala, “Microresonator soliton dual-comb spectroscopy,” Science **354**(6312), 600–603 (2016).
61. P. Pattnaik, “Surface plasmon resonance,” Appl. Biochem. Biotechnol. **126**(2), 079–092 (2005).
62. J. Homola, S. S. Yee, and G. Gauglitz, “Surface plasmon resonance sensors,” Sens. Actuators, B **54**(1-2), 3–15 (1999).
63. K. Matsubara, S. Kawata, and S. Minami, “Optical chemical sensor based on surface plasmon measurement,” Appl. Opt. **27**(6), 1160–1163 (1988).
64. W. Y. W. Yusmawati, H. P. Chuah, and M. Y. W. Mahmood, “Optical properties and sugar content determination of commercial carbonated drinks using surface plasmon resonance,” Am. J. Appl. Sci. **4**(1), 1–4 (2007).
65. J. Homola, “Present and future of surface plasmon resonance biosensors,” Anal. Bioanal. Chem. **377**(3), 528–539 (2003).
66. E. Wijaya, C. Lenaerts, S. Maricot, J. Hastanin, S. Habraken, J.-P. Vilcot, R. Boukherroub, and S. Szunerits, “Surface plasmon resonance-based biosensors: From the development of different

SPR structures to novel surface functionalization strategies," Curr. Opin. Solid State Mater. Sci. **15**(5), 208–224 (2011).

67. T. Kajisa, T. Yano, H. Koresawa, K. Otsuka, A. Sakane, T. Sasaki, K. Yasutomo, and T. Yasui, "Highly sensitive detection of nucleocapsid protein from SARS-CoV-2 using a near-infrared surface plasmon resonance sensing system", Opt. Continuum **1**(11), 2336-2346 (2022).
68. K. Tiwari and S. C. Sharma, "Surface plasmon based sensor with order-of-magnitude higher sensitivity to electric field induced changes in dielectric environment at metal/nematic liquid-crystal interface," Sens. Actuators, A **216**, 128–135 (2014).
69. H. Liang, H. Miranto, N. Granqvist, J. W. Sadowski, T. Viitala, B. Wang, and M. Yliperttula, "Surface plasmon resonance instrument as a refractometer for liquids and ultrathin films," Sens. Actuators, B **149**(1), 212–220 (2010).
70. C. E. H. Berger, T. A. M. Beumer, R. P. H. Kooyman, and J. Greve, "Surface plasmon resonance multisensing," Anal. Chem. **70**(4), 703–706 (1998).
71. R. Ziblat, V. Lirtsman, D. Davidov, and B. Aroeti, "Infrared surface plasmon resonance: a novel tool for real time sensing of variations in living cells," Biophys. J. **90**(7), 2592–2599 (2006).
72. A. Shalabney and I. Abdulhalim, "Figure-of-merit enhancement of surface plasmon resonance sensors in the spectral interrogation," Opt. Lett. **37**(7), 1175–1177 (2012).
73. H. Koresawa, K. Seki, E. Hase, Y. Tokizane, T. Minamikawa, T. Yano, T. Kajisa, and T. Yasui, "Beam-angle-scanning surface plasmon resonance sensor for rapid, high-precision sensing of refractive index and bio-molecules", Opt. Continuum **1**(3), 565-574 (2022).
74. R. Ziblat, V. Lirtsman, D. Davidov, and B. Aroeti, "Infrared surface plasmon resonance: a novel tool for real time sensing of variations in living cells," Biophys. J. **90**(7), 2592–2599 (2006).